Effect of Cryogenic Treatment on the Mechanical Properties of Nickel-Titanium Shape Memory Alloys

Stuart Brahm Kozlick

A Thesis

in

The Department

of

Mechanical and Industrial Engineering

Presented in Partial Fulfillment of the Requirements
for the Degree of Master of Applied Science (Mechanical Engineering) at
Concordia University
Montreal, Quebec, Canada

December 2013

CONCORDIA UNIVERSITY
School of Graduate Studies

This is to certify that the thesis prepared

By: Stuart Brahm Kozlick

Entitled: Effect of Cryogenic Treatment on the Mechanical Properties of Nickel-Titanium Shape Memory Alloys

and submitted in partial fulfillment of the requirements for the degree of

Master of Applied Science (Mechanical Engineering)

complies with the regulations of the University and meets the accepted standards with respect to originality and quality.

Signed by the final examining committee:

Dr. Nadia Bhuiyan Chair

Dr. Paula Wood-Adams Examiner

Dr. Michelle Nokken Examiner

Dr. Martin Pugh Supervisor

Approved by

Chair of Department or Graduate Program Director

Dean of Faculty

Date

ABSTRACT

Effect of Cryogenic Treatment on the Mechanical Properties of Nickel-Titanium Shape Memory Alloys

Stuart Brahm Kozlick

This experimental program investigated the effects of cryogenic temperature treatment on the mechanical properties and microstructure of Nickel-Titanium shape memory alloys. Mechanical testing including tensile and hardness were carried out after having undergone various cryogenic temperature treatment conditions, and the results were compared.

Experimental results showed an increase in material hardness was observed when compared to untreated materials. With both steady-state and cyclical conditioning, an increase of approximately 2.0% and 8.7% was observed, respectively. Furthermore, with respect to the cyclical temperature treatment exposures, an increase in both estimated final yield and tensile strengths was also observed, resulting in relative increases of 9.5% and 3.2%, respectively, when again compared to as-received materials. It was concluded these increases in mechanical properties were primarily due to both an increase in the formation of austenite throughout the material's microstructure, and the overall reduction in martensite grain size structure throughout the sample. The material's inherent twinning process of the microstructure, coupled with thermally stress-induced martensite plate growths at the martensite transformation temperature are potential contributors to this transformation in the microstructure, resulting in the observed change in mechanical properties.

ACKNOWLEDGEMENTS

First of all, I would like to extend my gratitude and appreciation to my supervisor, Dr. Martin Pugh for giving me the opportunity to perform research in the very interesting field of shape memory alloys. His excellent guidance, mentoring, and most importantly his friendship were instrumental in my development as a graduate student and my continued success as a professional. Many thanks go out to my fellow engineers and material scientists at Medtronic Inc. for their expertise and patience, in particular Thomas Miltich, Mallika Kamarajugadda, Paul Adler, and George Mallin. Sincere thanks go to Robert Oliver, Mazen Samara, and Charlene Wald of the Department of Mechanical and Industrial Engineering.

Lastly, I would like to thank my family and in particular my wife Jessica for their endless love and continued support.

TABLE OF CONTENTS

LIST OF FIGURES

LIST OF TABLES

CHAPTER 1

1.1 Introduction

1.1.1 Overview

This thesis considers the effects and influence of cryogenic temperatures on the mechanical properties and structure of shape memory alloys (SMA). Specifically, nickel-titanium alloys will be explored experimentally. This subject is motivated by the continued use of shape memory alloys in cryotheraputic devices in the medical device industry. Prolonged exposure to cryogenic temperatures and their effects thereof require a unique understanding in order to further develop and engineer upcoming medically and technologically advanced instruments.

1.2 Background

1.2.1 Active Catheters

A device that combines many aspects of instrument development for minimally invasive procedures is the active catheter. Catheters are long, thin, flexible tube-like instruments that are inserted in the patients groin, arm or neck, and advanced through vasculature to the site that requires investigation or treatment. Typical diameters range from 0.3 to 3mm, depending on the target vessel.

Although existing catheters in the hands of experienced physicians already save many lives today, they still suffer from limitations. The inability to reach the target vessel due to navigation and maneuvering difficulties is the most common problem in cardiovascular catheter treatment, and difficult cases associated with tortuous or difficult anatomical obstacles still challenge even the most experienced physicians. The placement of the catheter distal tip must always be carefully controlled from sometimes, more than one meter away by means of manipulating the distal end of the catheter which often is a very challenging task. In addition, in tortuous venous anatomy, there is a potential risk of vessel wall penetration, damage, or other trauma inflicted by the catheter. Even slight damage can cause tissue inflammation, which in turn can lead to potentially life-threatening vessel weakening, also known as aneurysms, or vessel blockage.

Enhancing catheters with steerable tips aims to ease the "steering problem", but since these steerable catheters are operated by "pull-wires", conventional steerable catheters require a high bending stiffness of the shaft in order to prevent buckling. This high stiffness requirement significantly increases the risk of damaging the vessel wall in bent sections. Recognizing this difficulty, research efforts are currently underway to integrate the capability of controlled steering into catheters, by exploiting micro-actuation techniques and "steer-by-the-wire" approaches. This is illustrated in Figure 1.1. A catheter that can be controlled to bend in any direction would also allow easier insertion, because it can follow the shape of the vasculature. Some medical device groups have even managed to integrate tactile sensors along with the micro-actuators that are able to detect contact with the vessel wall. Even though many prototypes have already been

conceptualized and developed, active catheter design still remains challenging. Further design improvements are required in order to attain optimal bending performance, rigidity, and device reliability before active catheters are entirely technically and economically feasible.

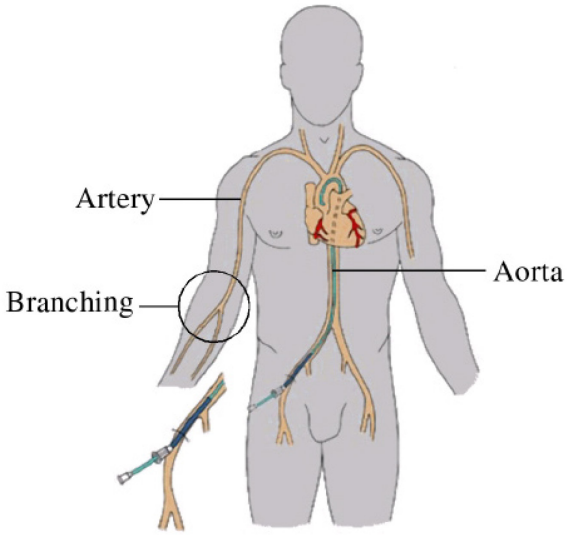

Figure 1.1 Illustration of cardiac catheterization [1].

1.2.2 Arrhythmias

An arrhythmia is an irregularity in the heart's normal rhythm. A recurrent arrhythmia is a condition that affects millions of people worldwide and is caused by a change or interruption in the way the heart receives and distributes electrical impulses.

Various types of arrhythmias exist depending on what part of the heart is affected and how they originate. The causes of arrhythmia also vary but can generally be divided into

two categories: (1) malfunctions in the electrical impulses that cause the heart muscle to beat; or (2) physical problems with the heart, such as valve disease, damage from a heart attack, or congenital heart defects. Untreated arrhythmias are a potentially serious medical condition. If left untreated, they can be the cause of serious heart problems and even lead to death. Early detection and treatment are crucial in preventing more serious health problems.

A common form of tachycardia which affects the atria is atrial fibrillation; this is a very common arrhythmia and is characterized by fast and uncoordinated beats of the atria, caused by the random contraction of individual heart-muscle fibers. Atrial fibrillation, also known as A-Fib or AF, is an irregular heart rhythm that affects the upper chambers of the heart. In A-Fib, the atria "quiver" instead of beating in a normal manner. A-Fib can also lead to rapid heart rhythm, where the heart can beat as much 300 times a minutes in the atria and up to 150 times a minutes in the lower chambers.

1.2.3 Cryotherapy

Cryotherapy, or cold therapy, is the local or general use of low temperatures in medical therapy. Its goal is to achieve a decrease in cellular metabolism, increase cellular survival, decrease inflammation, decrease pain and spasm, promote vasoconstriction (i.e., the narrowing of the blood vessels), and when using extreme temperatures, to destroy cells. Certain arrhythmias may be treated permanently with a technique known as

ablation. Performing cardiac ablation alters the abnormal electrical connection or impulse in the targeted heart cells and membranes in order to permanently interrupt the occurring arrhythmia. Depending on the type of arrhythmia and the patient's medical condition, this procedure may be performed with a catheter or, alternatively, during heart surgery. Different catheter-based ablation techniques may be used; they are categorized as follows: (1) cold-based procedures where tissue cooling is used to treat the arrhythmia, and (2) heat-based procedures where high temperatures are used to alter the abnormal conductive tissue in the heart.

Cryoablation is an innovative technique that restores normal electrical conduction by freezing tissue or heart pathways that interfere with the normal distribution of the heart's electrical impulses. By cooling the tip of the cryoablative catheter to sub-zero temperatures, the cells in the heart responsible for conducting the arrhythmia are altered so that they can no longer conduct irregular electrical impulses. Ablation occurs in tissue that has been frozen by at least three mechanisms: (1) formation of ice crystals within cells, thereby disrupting membranes, and interrupting cellular metabolism among other processes; (2) coagulation of blood causing an interruption of blood flow to the tissue, which in turn causes ischemia and eventual cell death; and (3) induction of apoptosis, a programmed cell death cascade [2].

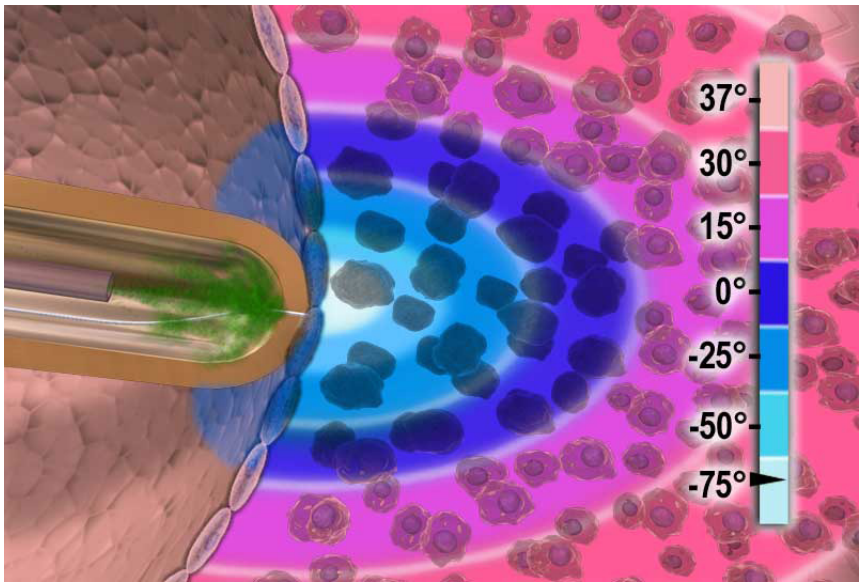

Figure 1.2 Thermal gradient; cryoablation using an active catheter [1].

1.2.4 Shape Memory Alloys

Certain metallic materials will, after an apparent plastic deformation, return to their original shape when heated. The same materials in a certain temperature range can be strained up to approximately 8% and still will return to their original shape when unloaded. These unusual effects are called thermal shape memory and superelasticity (elastic shape memory), respectively. Both effects depend on the occurrence of a specific type of phase change known as thermoelastic martensitic transformation. Shape memory and superelastic alloys respond to temperature changes and mechanical stresses in non-conventional ways. They are, therefore, sometimes called "smart materials". The shape memory effect can be used to generate motion and/or force, while superelasticity allows energy to be stored. Both effects have fascinated material scientists and engineers for decades drawing them to conferences and seminars in great numbers. However, very few developments have made it to market and can be considered economic successes. More

recent successes come mainly from medical applications utilizing the superelasticity and biocompatibility of nickel-titanium alloys, or nitinol alloys.

The shape memory effect as the result of martensitic transformation has been known since the 1950's, when the effect was discovered in copper-based alloys. In the early sixties, researchers at the Naval Ordnance Laboratory discovered the shape memory effect in Ni-Ti alloys (hence the name for these alloys - Nitinol -- Ni-Ti Naval Ordnance Lab) [3,4,5]. Today, these alloys are the most widely used shape memory and superelastic alloys, combining the shape memory effect, superelasticity, corrosion resistance, biocompatibility, and superior engineering properties. Copper-based alloys like Cu-Zn-Al and Cu-Al-Ni are also commercially available.

1.3 Scope of Research

1.3.1 Objective

The objective of this research is to explore the effects and influence of cryogenic temperatures on the performance and structure of shape memory alloys; specifically, nickel-titanium alloys. This objective is motivated primarily by the challenging nature of shape memory alloy designs, the lack of existing experimental work and knowledge of shape memory alloy design optimization, and thirdly, the expected benefit of structured and systematic design approaches for shape memory alloys. In particular, this work is aimed at upcoming future emerging applications that can utilize nickel-titanium shaped

alloy tubes to deliver cryogenic fluids, as well as to provide structural enhancements to active catheter probes that experience cryogenic environments. The main question that this research aims to answer is how and to what extent will the microstructure and mechanical properties of nickel-titanium shape memory alloy be affected by cryogenic temperature exposure.

CHAPTER 2

2.1 Introduction

Shape memory refers to the ability of certain materials to "remember" a shape, even after extensive deformations. After a permanent deformation of a shape memory alloy (SMA) structure, a temporary increase in temperature is sufficient to restore it back to its original state and shape. This effect is called the one-way shape memory effect, and is illustrated in Figure 2.1 by the curve A-B-C-D-E-A. This behavior is observed when the material is initially in the twinned martensite state. The loading causes detwinning of the initially twinned martensite, which leads to a relatively flat section (B-C) in the loading stress-strain curve. When the load is decreased after further elastic deformation of the twinned martensite (C-D), the unloading curve (D-E) differs from the loading curve (A-B-C-D). Hence, also in the stress-strain space hysteresis is generally observed. After removing the load, an apparently permanent deformation remains (E), as the detwinned martensite does not revert to the twinned state by itself, but remains in a new equilibrium configuration. By subsequent heating to a temperature above A_f, the phase transformation to austenite is triggered. As austenite has a cubic lattice which has no variants, this causes the material to recover its initial shape (A). This shape is maintained after returning to the (twinned) martensite state after cooling.

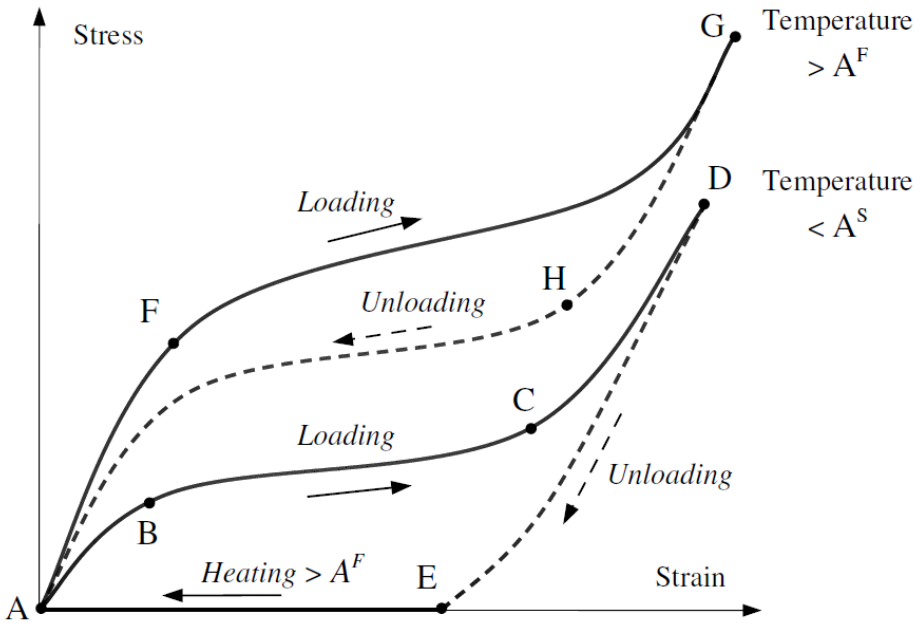

Figure 2.1 Schematic loading and unloading stress-strain curves for a typical shape memory alloy, at two different temperatures. The one-way shape memory effect is shown by the sequence A-B-C-D-E-A, and the superelastic effect by A-F-G-H-A [5].

Another effect, based on the same underlying phase transformation, is observed when the alloy is loaded in the austenite phase. The material in that case is able to elastically recover from quite large deformations (up to 8%). Normally, the elastic strain range for metals is nearly two orders less, at 0.1–0.2% [6,7]. This remarkable effect is known as superelasticity, or more correctly transformation pseudoelasticity. Pseudoelastic behavior is also depicted in Figure 2.1, by the curve A-F-G-H-A. The stressing of the material in its austenite state triggers the stress-induced phase transformation (F), which shows a similar plateau in the stress-strain curve as observed before.

At a certain load, all material has transformed into the detwinned martensite state (G). Upon unloading, however, the shape memory material transforms back to the austenite phase when the load has sufficiently decreased (H), and finally returns to its original shape when the load is completely removed (A). This ability to elastically recover large strains is often used in applications, next to the use of SMAs as actuator materials by the temperature-induced transformation. See for example Duerig et al. (1999) for an overview of medical applications of shape memory alloy superelasticity [3,4]. An overview of non-medical applications is given by Van Humbeeck (1999) [8]. Upcoming applications also include the use of shape memory alloy actuators in microsystems, using thin films produced by sputtering techniques. An extensive overview of recent developments in this direction is given by Fu et al. (2004) [9].

Designing shape memory alloy structures can be challenging mainly due to the complex stress-strain behavior inherent to the material. Moreover, shape memory alloy actuators are often controlled by direct resistive heating. Since these alloys are often controlled by resistive heating, electrical, thermal and mechanical aspects must all be considered.

2.2 Martensite: A Microscopic Perspective

Solid state transformations are typically of two types: diffusional and displacive. Diffusional transformations are those in which the new phase can only be formed by moving atoms randomly over relatively long distances [6,10]. This requires long range diffusion as the new phase that is formed is of a different chemical composition than the

matrix from which it is formed. Since this type of a transformation requires atomic migration, the diffusional transformation is dependent on both time, and temperature. Displacive transformations do not require large atomic migration. In this case, the atoms are rearranged into a new, more stable atomic structure in a supportive fashion [6,10]. This rearranging is done without changing the chemical nature of the matrix. Since no atomic migration is involved, these displacive transformations progress in a time independent fashion, with the motion of the surface between the two phases being limited only by the speed of sound. These transformations are also referred to as athermal transformations [6,10]. Martensitic transformations are of the displacive type, and are formed upon cooling from a higher temperature phase called the parent phase, also known as Austenite [3,11,12,13]. It is important to note that a precise definition of Martensite has never been agreed upon. The terms “Martensite” and “Austenite” are also used to refer to specific phases of steel. However, a more generalized definition for Martensite is based on the product of the phase transformation, rather than on a particular material (steel), and this is now in fact, more widely accepted.

Martensitic transformations are first order transformations; i.e., heat is liberated when Martensite is formed [14,15]. There is a hysteresis associated with the transformation and there is a temperature range over which Martensite and Austenite co-exists. Therefore it is possible to state that Martensite is formed upon cooling with the volume fraction of Martensite increasing as the temperature is reduced. It is important to note that the volume fraction is independent of time and is dependent solely on temperature.

From a crystallographic perspective, the phase transformation from Austenite to Martensite occurs in two parts: the Bain strain and the lattice invariant shear [6,14,16]. These mechanisms in a crystallographic sense are quite complex. The Bain strain, also referred to as lattice deformation, consists of all atomic movements that are needed to form the new structure (i.e., phase) from the old. Figure 2.2 illustrates the austenitic structure, and the progression of the transformation to a fully martensitic structure. It is important to note that the interface progresses through each atomic layer; each atom is required to move by only a very small amount resulting in the new martensitic structure. The movements that are required to produce the new structure are called Bain strain [14,17]. In more common materials, Bain strain generally consists of several atomic shuffles, in addition to the movement illustrated in Figure 2.2.

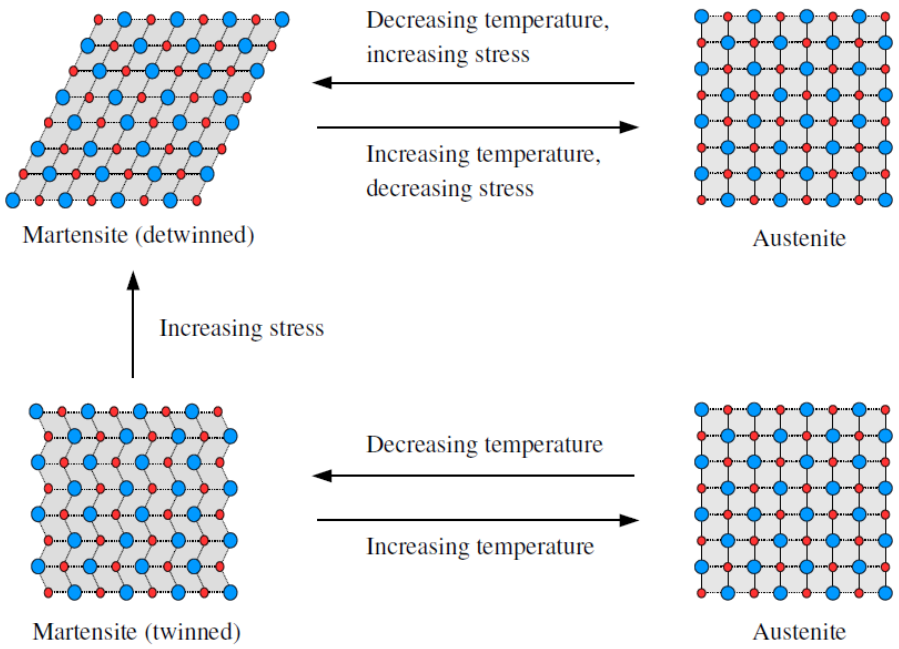

Figure 2.2 Transformation from Austenite to Martensite in two-dimensions; being completely austenitic, the interface advances - each layer of atoms is displaced only by a small distance, finally becoming completely martensitic [5].

The second part of a martensitic transformation is referred to as the lattice invariant shear [14,17]. Lattice invariant shear is an 'accommodation' step; the martensitic structure produced by the Bain strain is of a different shape, and often a different volume than the surrounding Austenite structure. Either the overall shape of the new phase or the surrounding Austenite must be altered in order to accommodate the new structure. There are two mechanisms by which this is possible: slip (Figure 2.3b) and twinning (Figure 2.3c) [6,11,14,18]. In both cases, each individual 'cell' has the new martensitic structure, but the overall shape is that of the original Austenite. Slip is a permanent process and is a common accommodation mechanism in many Martensite structures [6,14]. Twinning is unable to accommodate volume changes, but can accommodate shape changes in a reversible manner. In order for shape memory to occur to any significant extent, it is required that the accommodation be fully reversible; i.e., that twinning be the main accommodation process [14]. In Figure 2.3, only two directions or variants of shear are required to restore the original shape of the matrix.

The twinning process of accommodation plays a key role in the shape memory effect. The twin boundary is a mirror plane; when positioned on the boundary, the view in one direction is a mirror image of the other. Atoms located on that boundary see the same number and type of bonds in both directions. Key properties of twin boundaries are that they are of a very low energy and that they are quite mobile, therefore the stability of a martensitic phase is not strongly affected by the number or location of these boundaries [6,14].

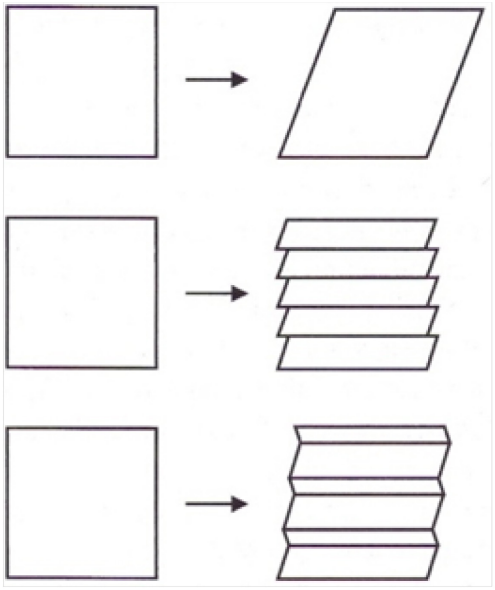

Figure 2.3 Phase changing to accommodate structure: (A) shape change upon martensitic transformation; (B) accommodation of strain by slip; (C) accommodation of strain by twins [4].

By comparing edges of the structures shown in Figures 2.3b and 2.3c, it can be observed that slip accommodation requires atomic bonds be broken, while all other bonds remain intact in the twinned structure. If a stress is applied to the structure shown in Figure 2.3c, the twin boundaries will easily move, resulting in a shape that better accommodates the applied stress. The result of moving a twin boundary is to convert one orientation or twin variant into another [4,6]. The variant chosen will be the one that is most oriented to the applied stress. In an ideal situation, a single variant of Martensite can be produced by straining a sufficient amount. This process of condensation of many twin variants into a single preferred variant is known as detwinning [3,4,14]. As previously described, only the twins within the individual martensitic plates have been considered thus far. However, crystallographic analysis has shown that the boundaries between martensitic plates also behave as twin boundaries themselves; i.e., the individual plates of Martensite

themselves are twins with respect to the adjoining plates [14]. Therefore, the term twin boundaries refer to both the boundaries between Martensite plates, as well as the boundaries within plates.

In Figures 2.1 through 2.3, the atom types have not been identified. In an alloy, however, there exist several species of atoms. It is therefore important to identify the lattice site locations of these atoms. In Nitinol, the atoms are ordered, meaning that the Ni and Ti atoms are found on specific sites, as can be seen in Figure 2.4 below [3,4,19]. During the martensitic transformation, the Martensite takes on the same ordering as the Austenite. This is referred to as inherited ordering. Shape memory alloys are generally based on a body-centered cubic (BCC) symmetry, some with the BCC structure, more often with the B2 structure, and some with an even more complex ordering called DO3, still based on the BCC symmetry [3,4].

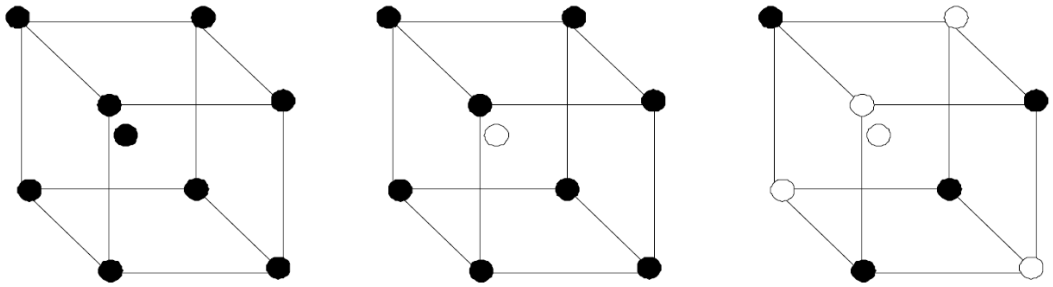

Figure 2.4 Ordered and disordered structures commonly found in shape memory alloys: (a) disordered BCC structure where different atom types are randomly distributed, (b) B2 structure, found mostly in Nitinol, where different atom types are found in specific locations, (c) higher order phase than (b) called DO3 state found for example in Cu-Al-Ni alloys [4].

Crystallographically, Martensite appears as plates resting planes known as habit planes. In many shape memory alloys, the Martensite plates are easily viewed through an optical microscope. Nitinol however exhibits fine plates that cannot be examined through an optical microscope [3,17]. It is therefore important to prepare samples for Nitinol microscopy very carefully since normal grinding and polishing techniques can sometimes disturb the Martensite.

2.3 Martensite: A Macroscopic Perspective

The physical properties of Austenite and Martensite are different. Therefore, as the phase transformation progresses and the transformation points are passed, a variety of property changes occur. Any of these property changes can be used to follow the progression of the phase transformation. There are four transformation temperatures that characterize the transformation process from Martensite to Austenite. Four temperatures indicated by M_s, M_f, A_s, and A_f (reference Figure 2.5) refer to temperatures at which the transformation to Martensite and Austenite start and finish, respectively. There exists a hysteresis associated with this martensitic phase transformation. The magnitude of the hysteresis varies from one alloy system to another, and has typical values ranging from 20°C to 40°C [3,20,21].

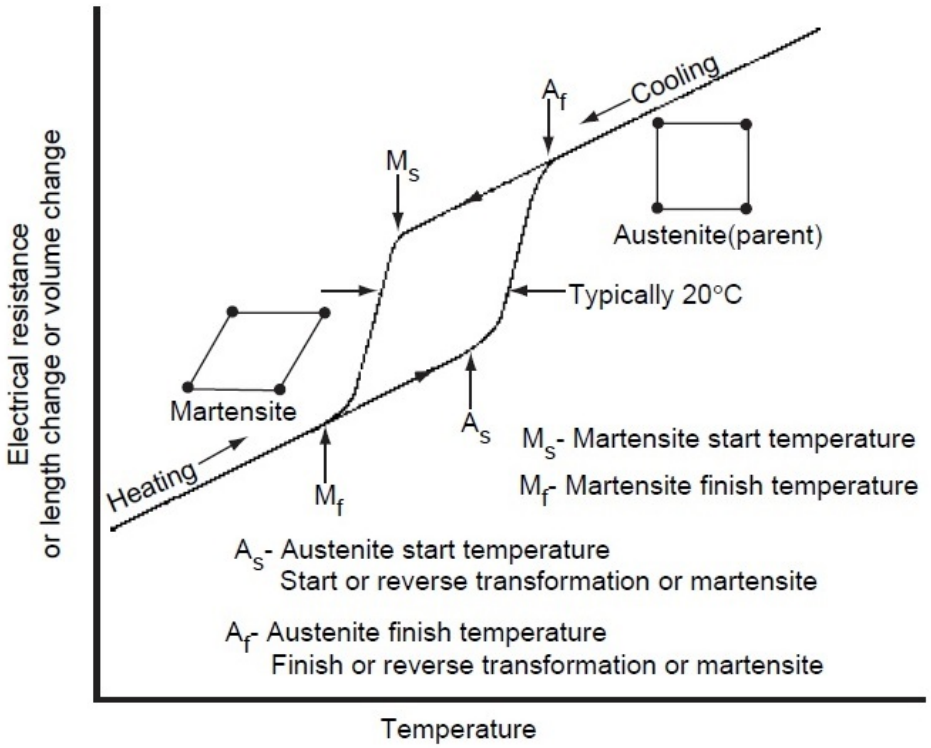

Figure 2.5 Property change versus temperature for a martensitic transformation occurring in a shape memory alloy [3,22].

One mechanical property that can change during the phase transformation is the materials yield strength. The martensitic structure deforms by moving twin boundaries. The twin boundaries are quite mobile, resulting in a martensite structure having low yield strength. Austenite on the other hand deforms by dislocation generation and movement [11,23]. Only a certain amount of martensite can be deformed based on a twin movement process and once this limit is exceeded, the material will again deform elastically, and eventually yield the second time around by virtue of an irreversible process; i.e., the movement of dislocations. The resulting tensile behavior is indicated in Figure 2.6. In Figure 2.6, the plateau is referred to as the thermal hysteresis, which means that both the Martensite and the Austenite are essentially controlled by the frictional stress of the twin boundaries. It is

the yield strength ratio between both the Martensite and Austenite structures that controls the ratio of resistances to reversible and irreversible deformations; i.e., twin movement to slip [5,11,24]. In shape memory alloys, it is important to have this ratio as high as possible in order to recover the most amount of the deformation. Typical values of these ratios are 0.1 to 0.2 [3,4].

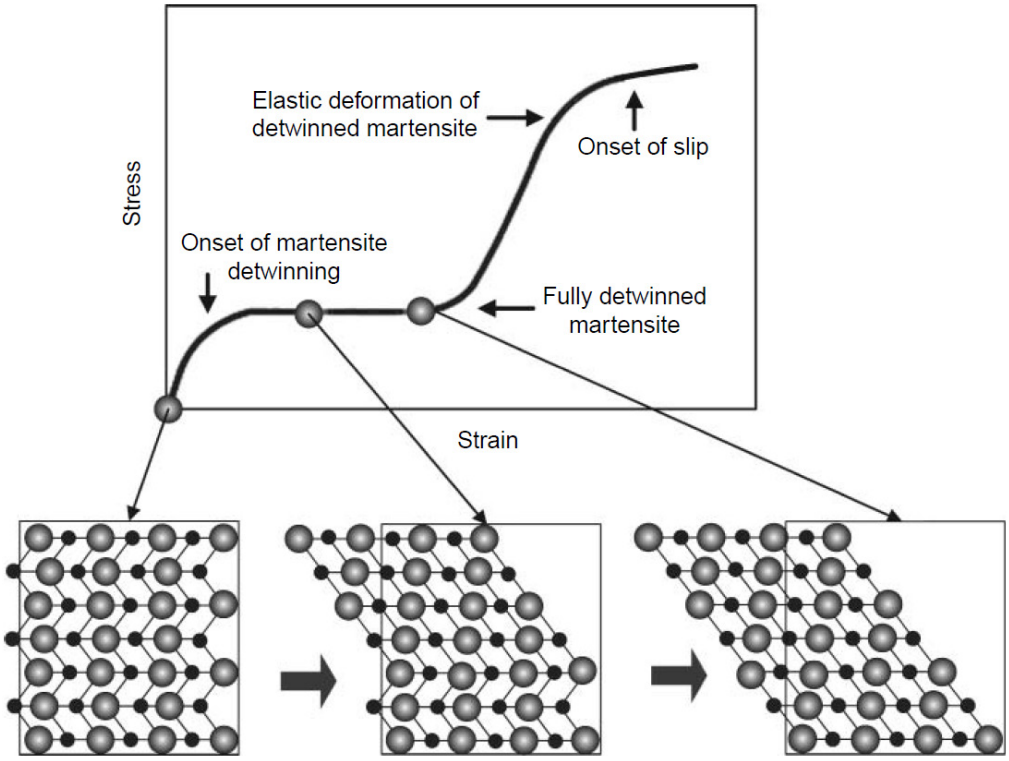

Figure 2.6 Stress-strain curve for a twinned martensitic material [5].

2.4 The Origin of Shape Memory Effect (SME)

Martensite is commonly of a lower symmetry than the Austenite phase. There are several methods by which Martensite can be formed out of Austenite. However, there is only one route by which the Martensitic structure that is formed will revert back to Austenite. The

shape memory effect can be explained in a very simple manner by a 2D geometrical concept depicted in Figure 2.7.

Upon cooling from Austenite, the self-accommodating variants of Martensite are formed. During the application of stress, the twin boundaries are capable of migrating and therefore can result in a biased distribution of Martensite variants. It is however important to note that no matter what distribution of Martensite exists, there is only one possible Austenitic structure that these variants can revert back to [4]. Therefore, the Martensitic variants must return back to the original undeformed shape when reverting back to the Austenite phase. Therefore, the shape accommodation due to a twin boundary movement can only be supported by a low symmetrical martensitic structure, and when the more symmetric Austenite structure is returned, the twinning deformation must also disappear [3,4,25,26].

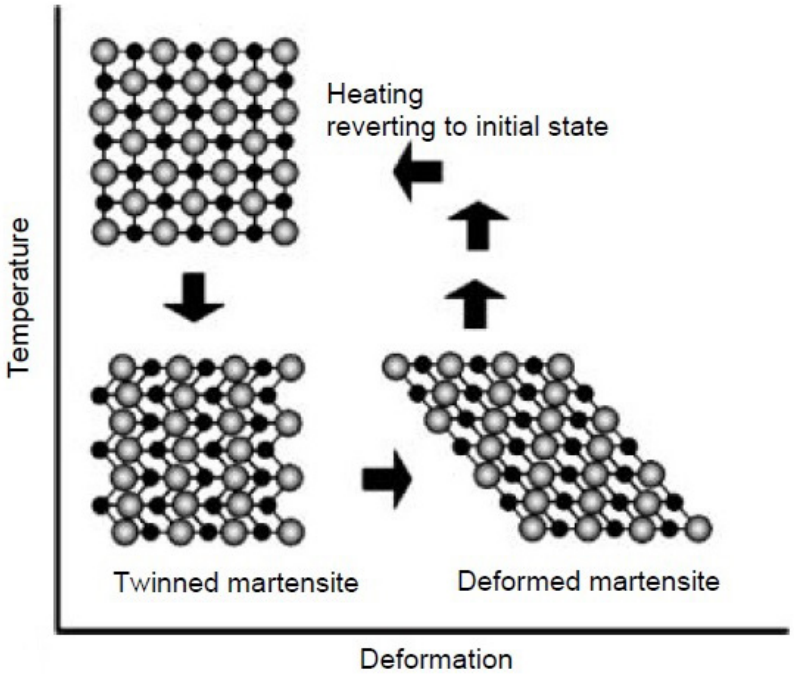

Figure 2.7 Shape memory shown microscopically: Austenite is cooled to form twinned Martensite, without undergoing a shape change, and then is deformed by moving twin boundaries. Heating either state will return the originally austenitic structure and shape [3,4].

2.5 Stress-Induced Martensite and Superelasticity (Pseudoelasticity)

Thus far, the shape memory effect has been considered to be both thermal and mechanical in nature. Martensite is primarily formed during cooling, deformed below the M_f temperature, and then heated to above the A_f temperature in order to cause the shape to recover. This implies that shape memory is caused by heating. There exists another type of shape memory that is dependent upon temperature, which is referred to as superelasticity. Simply put, the formation of Martensite is a thermoelastic process, which means that a decrease in temperature between both M_s and M_f will result in a slight growth of existing martensitic plates, in addition to the creation of new martensitic plates. This creation of new martensitic plates is also known as nucleation. However, when the

temperature is incrementally raised, the nucleated plates will disappear, and those which grew slightly upon incremental cooling, correspondingly, shrink back [14,17,27]. In other words, there exists an equivalence between temperature and stress; a decrease in temperature is equivalent to an increase in stress, and these both stabilize Martensitic structures.

The Martensite is also crystallographically reversible, which means, that the reversion of a given plate upon heating is simply the reverse of the formation process; i.e., the plates undergo a backwards shear as they disappear. Upon cooling, the Martensite forms under M_s if a stress is applied, and the formed Martensite is called stress-induced Martensite (SIM) [14,27]. The driving force for the transformation is in this case, mechanical rather than thermal. Above M_s, the stress required to produce stress-induced Martensite increases with increasing temperature.

The variation in stress required to produce stress-induced Martensite increases linearly with temperature above M_s. Figure 2.8 shows that the stress drops to zero at the temperature M_s. Again, because the martensitic transformation is a shear-like mechanism, stress assists in the martensitic transformation. Thus, it is possible to stress induce martensite even at temperature above M_s which is the highest temperature for the martensite to appear upon cooling.

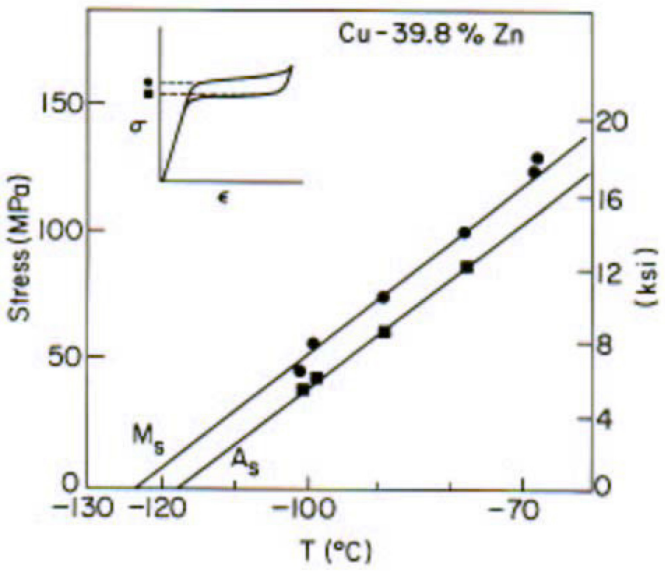

Figure 2.8 Stress plateau as a function of temperature [5,23].

The stress-induced martensitic transformation can be analyzed by the Patel–Cohen theory [3,4,28,29,30,31], in which the work done by an external stress on the system is treated to be equal to the change of the free energy of the system, and by the thermodynamic Clausius-Clayperon relationship [3,4,20,28,29,30,31], but the latter may be more easy to use, because it is summarized by the following:

$$\frac{dP}{dH} = \frac{\Delta H}{T\Delta V} \qquad (2.1)\ [3]$$

where P is the pressure, T is the temperature, and ΔH is the transformation latent heat and ΔV is the volume change of the phase transformation. Equation 2.1 has been traditionally used by chemists, however metallurgical and material science engineers will utilize the Clausius-Clayperon equation in the following format:

$$\frac{d\sigma}{dM_s} = \frac{\Delta H}{\varepsilon_0 T} \qquad (2.2)\ [3,20,29]$$

where ΔH and T have the same interpretation as for Equation 2.1, σ is the applied stress, M_s is the shifted M_s temperature, and ε_0 is the transformational strain resolved along the direction of the applied stress.

The difficulty to stress induce Martensite continues to increase with temperature until M_d, M_d being the temperature above which the critical stress required to induce Martensite is greater than the stress required to move the dislocations [3,4,20,29]. M_d is sometimes also referred to as the martensite deformation temperature. Therefore, the temperature range for stress-induced Martensite is from M_s to M_d [3,20,29,31]. For a number of shape memory alloy systems, the agreement in the temperature dependence of the stress to form stress-induced Martensite according to the Clausius-Clayperon equation is quite striking. The equation works similarly for the non-isothermal case; i.e., the case where temperature would be held constant, while the stress needed to form Martensite was measured.

Superelasticity occurs when a material is deformed above A_f, but still below M_d [3,4,32]. In this temperature range, Martensite can be made stable with the application of stress, but becomes unstable upon its removal. This narrow range is dependent on the material's respective strain. As an example, Figure 2.9 introduces some of the key parameters linked to superelasticity. Residual strain is the strain that is not immediately recovered upon loading. This is also known as the *set*. The set that results from a superelastic deformation may be permanent, thermally recoverable, or a combination of the two, all depending on

the deformation temperature and strain. Springback strain consists of three contributors: the elasticity of the Austenite, the elasticity of the Martensite, and the phase transformation itself. Two plateau stresses are also depicted in Figure 2.9: loading and unloading plateaus, or upper and lower plateaus, respectively. These plateaus are related to the nonlinear and nonconservative tensile properties inherent in the material. These two properties and their respective curves provide the material with another property known as biased stiffness [3,8,32,33]. Biased stiffness is best understood by imagining that the material stops unloading somewhere on the unloading plateau (solid curve), followed by further unloading that continues down the solid curve and is highly compliant, whereas resistance to deformation follows a normal elastic loading curve. This normal loading is comparatively very stiff.

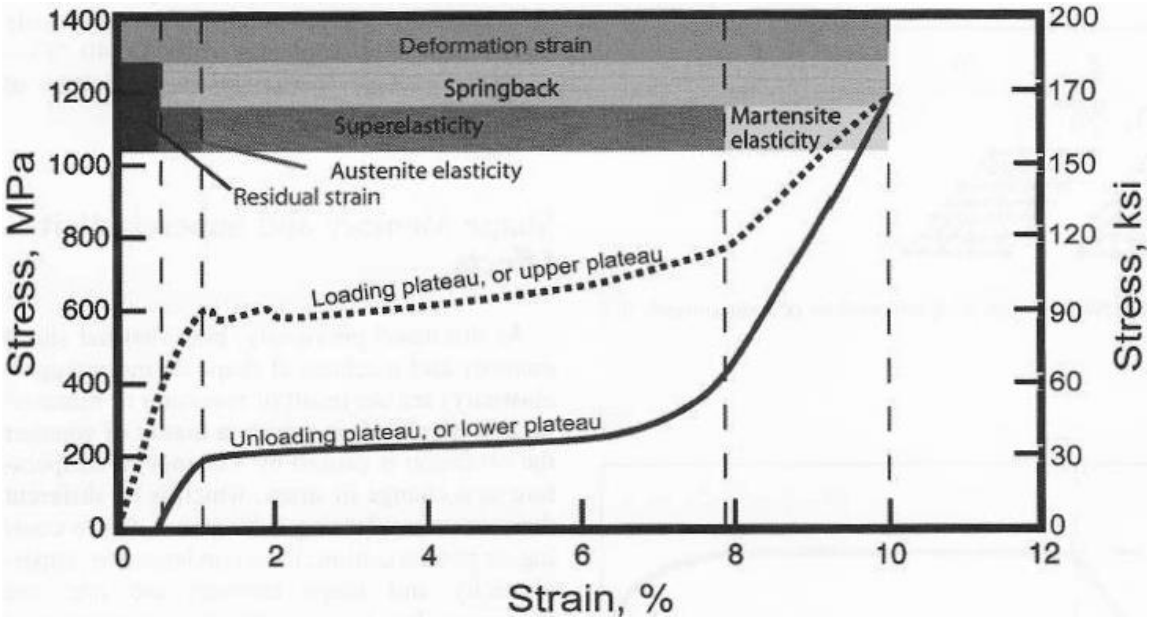

Figure 2.9 Stress-strain for a superelastic shape memory alloy, loaded beyond the point at which it is able to completely recover. Springback strain is partitioned into elastic recovery of martensite, recovery of the transformational strain of martensite to austenite, and the elasticity of austenite [3,4,14].

2.6 Martensitic Transformation

2.6.1 Linear Algebra describing the Crystallographic Deformation

When a deformation is linear, the deformation can be represented by the following:

$$\begin{pmatrix} x_2 \\ y_2 \\ z_2 \end{pmatrix} = \begin{pmatrix} a_{11} & a_{12} & a_{13} \\ a_{21} & a_{22} & a_{23} \\ a_{31} & a_{32} & a_{33} \end{pmatrix} \begin{pmatrix} x_1 \\ y_1 \\ z_1 \end{pmatrix} \quad (2.3)\ [34,35]$$

This can then be represented by

$$r_2 = Ar_1 \quad (2.4)\ [36]$$

where A represents the matrix a_{ij}. In other words, any vector r_1 is transformed into r_2 by a matrix A as an operator. Using linear algebraic principles, a coordinate transformation is necessary since we refer to both the parent phase and the martensitic phase, which could both have different structures. Suppose we model in two axis systems represented by the base vectors *a, b, c* (considered the original system) and *A, B, C* (considered the new system). We can write the relations between both systems as

$$\begin{aligned} A &= s_{11}a + s_{12}b + s_{13}c \\ B &= s_{21}a + s_{22}b + s_{23}c \\ C &= s_{31}a + s_{32}b + s_{33}c \end{aligned} \quad (2.5)\ [4,36]$$

We then solve for *a, b, c* as functions of *A, B, C*, and we obtain the following:

$$\begin{aligned} a &= t_{11}A + t_{12}B + t_{13}C \\ b &= t_{21}A + t_{22}B + t_{23}C \\ c &= t_{31}A + t_{32}B + t_{33}C \end{aligned} \quad (2.6)\ [36]$$

Furthermore, if we expand this mathematical approach a little further, there are two more transformation formulas for vector components in direct and in reciprocal space that can be written, and they are

$$\begin{pmatrix} x \\ y \\ z \end{pmatrix} = \begin{pmatrix} s_{11} & s_{12} & s_{13} \\ s_{21} & s_{22} & s_{23} \\ s_{31} & s_{32} & s_{33} \end{pmatrix} \begin{pmatrix} X \\ Y \\ Z \end{pmatrix} \qquad \text{(2.7) [4,17,36]}$$

old A B C new

and

$$\begin{pmatrix} H \\ K \\ L \end{pmatrix} = \begin{pmatrix} s_{11} & s_{12} & s_{13} \\ s_{21} & s_{22} & s_{23} \\ s_{31} & s_{32} & s_{33} \end{pmatrix} \begin{pmatrix} h \\ k \\ l \end{pmatrix} \qquad \text{(2.8) [4,17,36]}$$

old new

where the *xyz* and *XYZ* refer to the direct lattice, and *hkl* and *HKL* to the reciprocal lattice, respectively [4,14,17]. It is important to recall from matrix algebra that when a coordinate transformation is applied for a vector or a plane, an operator is also transformed following the similarity transformation, given by

$$\begin{aligned} \overline{A} &= R^{-1} A R \quad \text{or} \quad A = R \overline{A} R^{-1} \\ \overline{A} &= R^{\mathrm{T}} A R \quad \text{or} \quad A = R \overline{A} R^{\mathrm{T}} \end{aligned} \qquad \text{(2.9) [36]}$$

where A is an operator in the original system, $\overline{A}$ is with respect to the new system, R is a rotation matrix, R^{-1} is the inverse of R, and R^{T} is the transpose of R.

2.6.2 Structural Change without Diffusion

We can now discuss how the martensite crystal is produced from the parent crystal without diffusion. We can describe this for FCC (Face Centered Cubic) and BCT (Body Centered Tetragonal) transformations in steels. Figure 2.10a shows two FCC unit cells where a BCT lattice is present with the axial ratio $c/a = \sqrt{2}$ [4,6,7].

If the *X* and *Y* axes in Figure 2.10a are lengthened and the *Z* axis is contracted so that *c/a* becomes the value of the martensite, a value close to 1, then a BCT martensite structure is created, as shown in Figure 2.10b [4,17]. Though the method is different from one alloy to another, it is possible to produce a martensite structure from a parent by the combination of elongation, contraction, and shear along certain directions.

If the lattice parameter of the FCC is a_0, and those of the BCT are a and c, then the lattice deformation with respect to the *XYZ* axes is written as:

$$B = \begin{pmatrix} \sqrt{2}a/a_0 & 0 & 0 \\ 0 & \sqrt{2}a/a_0 & 0 \\ 0 & 0 & c/a_0 \end{pmatrix} \qquad (2.10)\ [4,14,17,36]$$

By using the similarity transformation derived in equation (2.9), the lattice deformation matrix with respect to the parent lattice, the *xyz* axes in Figure 2.12a, is given as follows:

$$B = R\bar{B}R^{\mathrm{T}} = \begin{pmatrix} 1/\sqrt{2} & 1/\sqrt{2} & 0 \\ -1/\sqrt{2} & 1/\sqrt{2} & 0 \\ 0 & 0 & 1 \end{pmatrix} \begin{pmatrix} \sqrt{2}a/a_0 & 0 & 0 \\ 0 & \sqrt{2}a/a_0 & 0 \\ 0 & 0 & c/a_0 \end{pmatrix} \begin{pmatrix} 1/\sqrt{2} & -1/\sqrt{2} & 0 \\ 1/\sqrt{2} & 1/\sqrt{2} & 0 \\ 0 & 0 & 1 \end{pmatrix} \quad (2.11)\ [36]$$

Furthermore, another important concept is the lattice correspondence, which is associated with the lattice deformation. Since martensitic transformations are diffusionless, there is a one-to-one correspondence in the directions and planes between and the parent and the martensite [4,14,36].

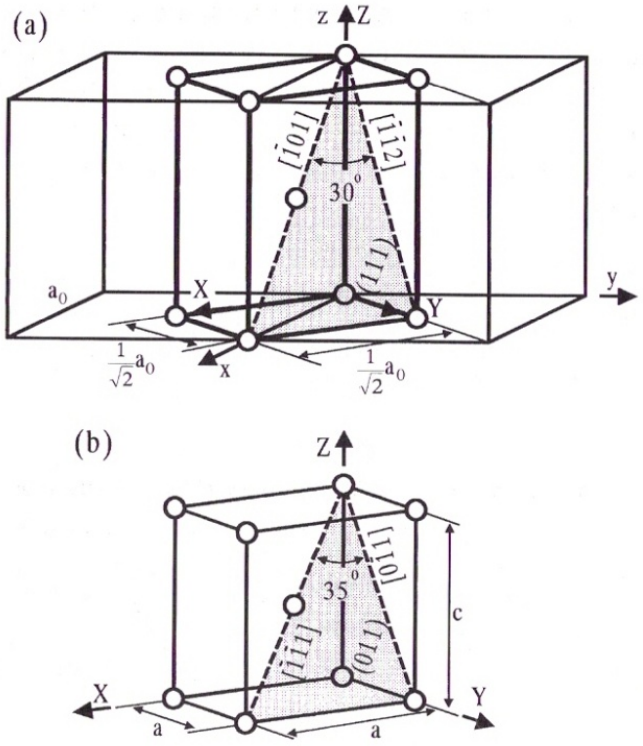

Figure 2.10 Mechanism of FCC-BCT transformation; xyz represent the crystal axes in the parent FCC lattice, while XYZ represent the axes in the BCT martensite [4].

2.7 Types of Shape Memory Effects

2.7.1 One-Way Shape Memory Effect

The shape memory effect is a consequence of the fact that isothermal shape change due to pure reorientation can be undone by thermal reverse martensitic transformation. In particular, starting with austenite, consider a three stage cycle (Figure 2.11) composed as:

- (sm1) thermal forward martensitic transformation (i.e., A → M by cooling in the absence of stress) [20,37];
- (sm2) isothermal reorientation M → M+ due to loading which then persists upon unloading [20,37];
- (sm3) thermal reverse martensitic transformation (i.e., M+ → A by heating in the absence of stress) [20,37].

Stage (sm1) gives no shape change, whereas stage (sm2) provides a plastic deformation. However, stage (sm3) reverses the shape change by thermal means, producing the shape memory effect. At the conclusion of (sm3), the material has returned to the shape associated with the original austenite and remains at that shape during any temperature change (even a cooling associated with forward martensitic transformation) so long as there is no further loading, as depicted in Figure 2.11.

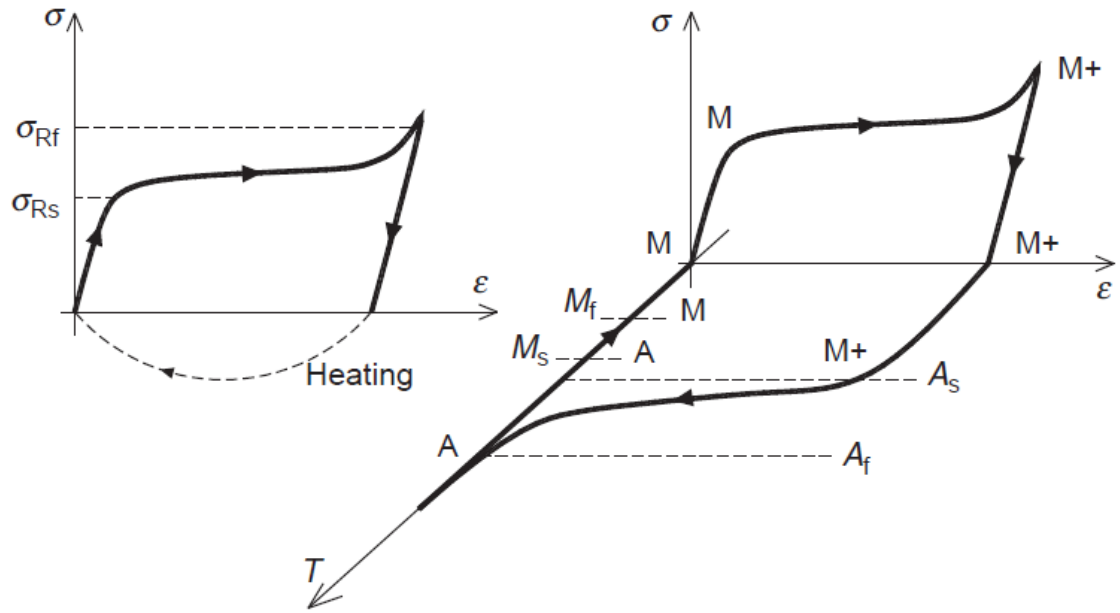

Figure 2.11 For T < Mf, loading and unloading reorients an originally self-accommodated martensite, resulting in an apparent plastic strain. Heating converts the reoriented martensite to austenite, returning the material to its original shape (the shape memory effect) [5].

The two-way memory effect refers to certain processes wherein multiple cycles of this kind are performed in such a manner so as to create a defect structure (e.g., a dislocation pattern) after reorientation that serves to stabilize the deformation after stage (sm2). This "training" can lead to a situation where the shape change associated with reorientation can be obtained by cooling with no application of load, at which point a stress-free cooling and heating cycle gives a reversible shape change [3,20]

2.7.2 Two-Way Shape Memory Effect

Two-way shape memory (TWSM) can be trained into a shape memory alloy by the process of thermomechanical cycling. The process of training will generally result in the

alloy remembering both its low and high temperature shapes. TWSME depends solely on temperature, which means that a change in temperature will cause changes in shape. The shape memory alloy will also remember its 'intermediate' shapes in addition to the shapes it assumes at the high and low temperatures [3,38,39,40].

In one-way shape memory effect, after the completion of individual cycles of deformation and heating, the alloy must be re-deformed to repeat the SME. In TWSM, only temperature must be varied in order to affect the change in shape [38,39]. The amount of strain recovery is however lower in TWSM than in one-way shape memory effect. Shape memory alloys that have been trained are also referred to in general literature as "educated" [38,39]. Thermomechanical fatigue is essential for the completion of the education of the shape memory alloy. However, it can have undesirable effects like elevation of the transformation temperatures, widening of the hysteresis loop, and an increase in the levels of residual strains. As depicted in Figure 2.12, a collapsed shape memory alloy sample spring (contracted) is recovered following heating to above A_f. The contracted spring remains when the specimen is again cooled below M_f. This is the one-way shape memory behavior, which is a onetime only deployment. In contrast, two-way shape memory is depicted in the lower half of Figure 2.12, in which case a contracted spring extends when heated to above A_f, but now contracts when cooled again below M_f and this can be repeated indefinitely.

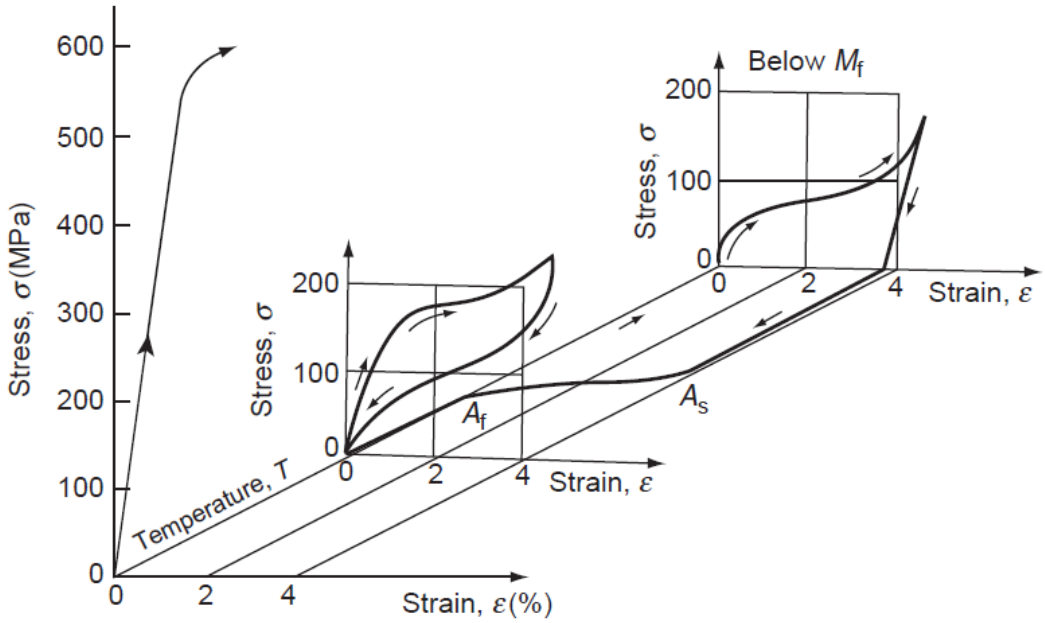

Figure 2.12 Three-dimensional plot of stress, strain, and temperature for a sample shape memory spring, with temperature increasing into the page [38,39,40]. The closest curve shows elastic and plastic deformation of austenite which occurs if the temperature is above M_d. The middle curve displays the behavior that takes place below M_d, but above A_f, commonly referred to as superelasticity. The final part of the schematic displays the entire path taken for the limiting case of shape memory. Following the arrows in the diagram, the sample is cooled to M_f, deformed, unloaded, and heated through A_s to a temperature above A_f for strain full recovery [3,38,39,40].

2.8 Nickel-Titanium Shape Memory Alloys

2.8.1 Introduction

Shape memory alloys based on Nickel and Titanium provided the best combination of material properties for most commercial applications. Rapid growth for shape memory alloys was initiated with the discovery of shape memory properties in Ni-Ti systems in the 1960's [3,4,5].

2.8.2 Metallurgy of Nickel-Titanium Alloys

Nickel-Titanium shape memory alloys are ordered intermetallic compounds based on equiatomic composition. Referencing the phase diagram for Ni-Ti in Figure 2.13, this compound exists as the stable phase down to room temperature. In contrast to copper-based alloys, it is not necessary for any betatising and quenching in order to prevent decomposition of NiTi into other phases at intermediate temperatures [41]. At low temperatures, the stoichiometric range of NiTi is very narrow and therefore the alloys often contain precipitates of a second intermetallic phase [16,19,41]. The microstructure is thus primarily single phase, with small amounts of other phases mixed in the matrix. In its molten state, Titanium is very reactive and this results in some oxygen potentially being present in the matrix.

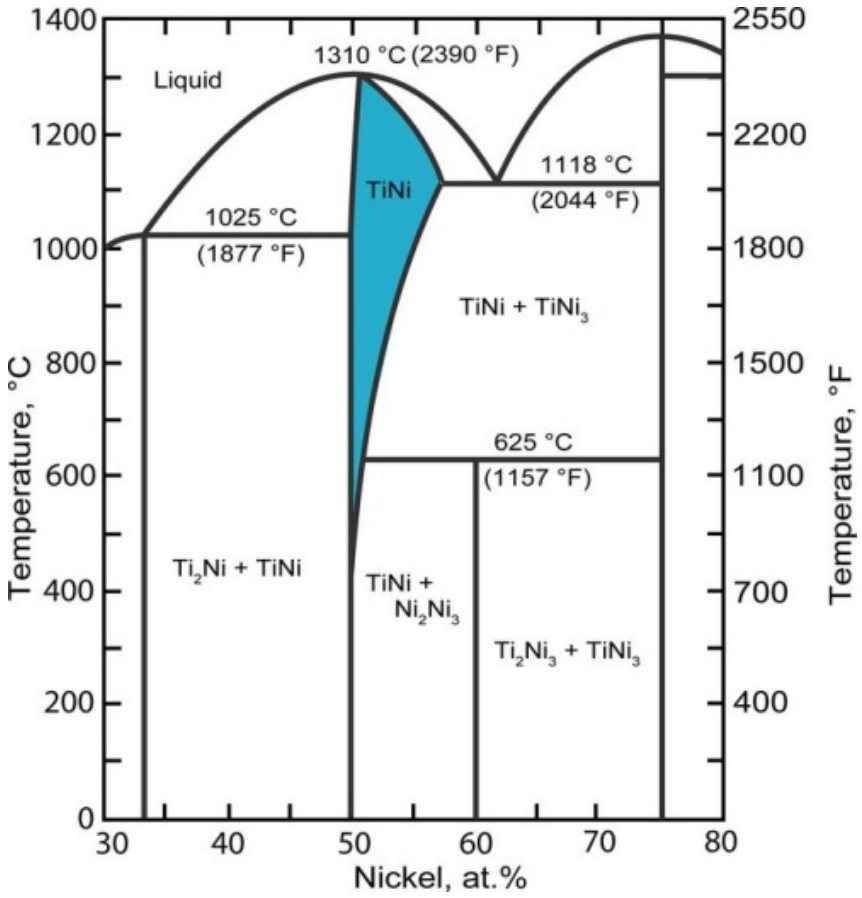

Figure 2.13 Typical phase diagram of nickel-titanium alloys [41,42].

In NiTi alloys, the transformation temperature M_s is strongly dependent on the oxygen content and composition. For example, increasing the oxygen content from 150 ppm (parts per million) to 450 ppm decreases the M_s temperature from 45°C to -5°C. The composition sensitivity of NiTi is of considerable importance and requires precise composition control during alloy preparation. Depending on the desired M_s, the necessary control is between 0.01 and 0.1% [5,43].

Standard NiTi alloys show a hysteresis of 30–50°C but, with modifications, it is possible to either extend this to over 100°C or reduce it to about 10–15°C or even to 0–5°C in the

case of some NiTi alloys with a pre-martensitic transformation, commonly known as the R-phase [3,41,44].

The R-phase is a rhombohedral phase of Nitinol that forms from the cubic austenite phase and is considered another martensite crystal structure. The R-phase possesses both shape memory and superelastic effects, although are much smaller than the native martensite structures [3,4]. The R-phase completes with austenite and martensite phases energetically, and can sometimes appear before martensite is formed upon cooling, as well as before austenite is formed upon heating [5].

The addition of third or fourth elements to NiTi alloys provides a useful tool in controlling the alloy's transformation temperatures, increasing the stability of M_s, controlling the hysteresis width, increasing austenitic strength, reducing or increasing martensitic strength, and improving corrosion resistance. Additions of Cu, Nb and precious metals provide a useful combination of properties [17]. For example, the addition of copper can reduce the alloy's respective hysteresis width and composition sensitivity to the transformation temperature M_s and improve the fatigue resistance. Furthermore, the Cu-containing ternary NiTi alloy also has a martensite phase with a lower yield strength, thus requiring a lower reset force for some cyclic applications. Alloys with 10% Cu exhibit a two-step transformation and a corresponding two-step shape change [3,17,41].

NiTi alloys have excellent corrosion resistance which is provided by a naturally formed thin oxide layer or "passive film". The stability of this film provides NiTi alloys with good resistance to many forms of corrosive attack. Different physical and shape memory properties of NiTi-based alloys are shown in Table 2.1.

Table 2.1 Properties of nickel-titanium alloys [3,5].

Physical Property	**Value (martensite (M) / austenite (A)**
Melting Point (ºC)	1310
Density (g/cm^3)	6.5
Electrical resistivity (μΩ-cm)	76 (Martensite) | 82 (Austenite)
Thermal Expansion (10^{-6}/ ºC)	6.6 (Martensite) | 11 (Austenite)
Thermal Conductivity (W/(m.K))	18

2.8.3 Mechanical properties

For orthopedic biomaterial applications, the two properties of major importance are strength (mechanical) and reactivity (chemical). Generally, there are two basic mechanical demands for the material and design of the implant. Service stresses must be safely below the yield strength of the material, and in cyclic loads the service stress must be kept below the fatigue limit.

Mechanical properties of NiTi principally depend on its phase state at a certain temperature. Fully austenitic NiTi material generally has suitable properties for surgical implantation applications [1,2]. The common mechanical properties of martensitic and austenitic NiTi are presented in Table 2.2 below. There exist some exceptional properties

that might be useful in surgery. For example, NiTi has an ability to be highly damping and vibration-attenuating below A_s. From an orthopedic point of view, this property could be useful in dampening the peak stress between mated bone, and the articular prosthesis. The low elastic modulus of NiTi, which in reality is much closer to the elastic modulus of bone, might provide large benefits in specific applications. NiTi has unique high fatigue and ductile properties, which are also related to its martensitic transformation.

Table 2.2 Selected mechanical properties compared between nitinol, stainless steel (316LVM), titanium (cp-Ti, grade IV), and Ti6Al-4V alloy [1,2,3,5,19].

Mechanical Property	**Nitinol**		**Stainless Steel (316LVM)**	**Titanium (cp-Ti, grade IV)**	**Ti-6AL-4V**
	Austenitic	**Martensitic**			
Tensile Strength (MPa)	800-1500	103-1100	483-1850	540-740	920-1140
~ Yield Strength (MPa)	100-800	50-300	190-1213	390	830-1070
~ Final Elastic Limit Yield Strength (MPa)	68-1280				
~ Modulus of Elasticity (GPa)	70-110	27-82	190-200	105-110	100-110
Elongation at failure (%)	1-20	Up to 60	12-40	16	8

These properties are usually favorable in orthopedic implants. NiTi also exhibits very high wear resistance. NiTi is a non-magnetic alloy, allowing for MRI imaging. Electrical resistance and acoustic damping also change when the temperature changes.

2.8.4 Designing for Nitinol

2.8.4.1 Ability to Recover Large Deformations

Mechanical strain reaching up to 8% can be recovered either via thermal shape memory or superelasticity. This characteristic is extensively valuable as it allows compact designs, small delivery systems, larger installation or insertion clearances. It also allows a confined entry through narrow cannulas, trocar ports, catheters and other percutaneous access devices. Once recovered inside the patient's body cavity, the nitinol component can be used to steer, bend, twist, deploy, and/or expand [1,2].

2.8.4.2 Kink and Crush Resistance

Both kink and crush resistance refer to the ability to resist a permanent deformation under a certain amount of strain. Superelastic NiTi is superior to other alloys typically used in the medical device industry like stainless steels and titanium alloys and makes it a material of choice for a large number of surgical, guidewire or stent applications where kink or crush resistance are essential.

Kink and crush resistance are directly proportional to superelasticity therefore one must ensure that the application or design fit well within the superelastic temperature range [1,2]. This superelastic temperature range is highly sensitive to heat treatment conditions. Both superelastic range and fatigue properties benefit from high ultimate tensile strength

to loading plateau stress ratio. Because of these temperature dependencies, design and manufacturing must focus on both the device use and operating conditions.

2.8.4.3 Flexibility, Torqueability, and Pushability

Flexibility is the ability of a material to deflect elastically under low stresses. Inversely proportional to stiffness, flexibility can be enhanced with proper thermomechanical processing of the alloy; i.e., increase the amount of cold work to decrease modulus for example or aging treatment and/or geometric variations [1,2,43].

Torqueability is the ability of a material to transfer a twisting or rotating action from one end to the other under some level of constraint. It is a function of both geometrical and microstructural integrity of the material and the constraint strain. For NiTi alloys, processing parameters such as time, temperature and tension in the production of a straight product play a key role in attaining a torqueable component [1,2,43]. In most cases and size for size, NiTi is far less torqueable than stainless steel.

Pushability is the ability of a material to transfer a longitudinal motion throughout its length without significant lateral deflection and/or buckling. It is important to understand that this quality is defined by the stiffness or elastic modulus of the material, and not the superelastic loading plateau stress although it may be perceived as such because of a subjective ‘feel’ in the hands of the user. This characteristic is sensitive to processing

parameters such as amount of cold work and annealing conditions as well as operating temperature [1,2,43]. Geometrical parameters, such as straightness, are also important.

2.8.5 Design Challenges and Difficulties

2.8.5.1 Non-linear Behavior

The non-linear elastic and thermo-elastic behaviors of nitinol alloys hinder accurate modeling and analysis. They also make the more subjective 'feel' so critical to physicians manipulating a device which is an extension of their hand, a very foreign experience. Familiar Hookean elasticity and plastic yield concepts no longer apply.

Because of this non-linear elastic behavior, the material can accumulate and restore a tremendous amount of potential energy that could be extremely deceiving and lead to premature failure or malfunction of the device [1,2]. One could imagine a surgical guidewire prevented from rotating by a very tortuous vascular pathway or a kink, and the energy that the user could potentially store in the wire while continuing to torque it. The wire could either break within a patient's arteries or unwind, causing serious injury to the vasculature.

2.8.5.2 Stress Hysteresis

The stress hysteresis between the loading and unloading plateau stresses of superelastic nitinol alloys can be used advantageously. In an endoluminal stent application for example, the high loading plateau stress increases the crush resistance of a stent placed in superficial arteries, and in articulated areas when stents are under a lot of external loading configurations. Manufacturing wise, the high plateau stress has to be overcome for compression and insertion in a delivery or constraining system leading potentially to frictional resistance and other assembly issues [43]. The usually much lower unloading plateau stress assists in preserving a gentle external pressure against the wall of the vasculature, and minimizes the vessel's respective recoil.

2.8.5.4 Thermal Hysteresis

The difference between the martensitic transformation paths needs to be accounted for when designing with nitinol alloys. The constant 37.5°C body temperature allows using the thermal hysteresis effectively not only in a variety of device applications, but also during manufacturing or assembly. This hysteresis can be used advantageously from a design or manufacturing perspective by ensuring its position in relation to body temperature by either selecting the right material chemical composition or thermo-mechanical processing [1,2,3]. As an example, with an arterial stent in its expanded state (austenitic shape), initially it is cooled down and mechanically crushed into a smaller diameter, allowing for insertion, first into the delivery system sheath and then into the patient's vasculature (martensitic shape). During insertion, the stent does in fact warm up

given the surrounding temperature but remains crushed inside the delivery system sheath. During delivery and once the sheath is removed, the stent self-expands, recovering its initial austenitic shape.

CHAPTER 3

3.1 Experimental Methodology

3.1.1 Overview

This chapter explains the experimental procedure approach for the cryo-temperature thermal treatment and evaluation of medical device Nitinol (ASTM F2063-05). This study investigated the effect of cryo-temperature preconditioning and exposure on the mechanical properties of nickel-titanium shape memory alloys by comparing different exposure durations and cycles of cryo-temperatures. Material property testing, including tensile testing and microhardness testing were performed. Material microstructural analyses were executed using scanning electron microscopy. Fracture surface analysis was performed using digital microscopy and scanning electron microscopy. Material thermoanalytical analysis was carried out using a differential scanning calorimeter.

3.2 Experimental Approach

3.2.1 Experimental Test Plan – Version 1

Flowchart 3.1 outlines the test plan originally devised for this research. In this study, five different temperature treatment sequences were designed to evaluate the response of the nitinol material. The cryo-temperature exposure sequences were selected and further evolved based on clinical relevance during a typical cryoablative cryotherapy procedure. They included:

a) Baseline room temperature samples – these will act as control samples;

b) Exposure to -60°C for a duration of 32 minutes; clinical relevance equivalent to that of two, four minute cryotherapy treatment applications to four pulmonary veins located in the left atrium of the heart. This can be seen as a minimal treatment provided in a cryotherapy procedure.

c) Exposure to -60°C for a duration of 64 minutes; clinical relevance equivalent to that of four, four minute cryotherapy treatment applications to four pulmonary veins located in the left atrium of the heart. This can be seen as a maximum-duration treatment provided in a cryotherapy procedure.

d) Exposure to -60°C for a duration of 128 minutes; theoretical clinical relevance equivalent to that of eight, four minute cryotherapy treatment applications to four pulmonary veins located in the left atrium of the heart. This can be seen as an extraneous treatment provided in a cryotherapy procedure.

e) Cyclical exposure: +37°C exposure for a duration of 4 minutes, followed by -60°C for a duration of 4 minutes and repeat cryo-exposure four times; total cyclical preconditioning is 32 minutes. The clinical relevance of the cyclical type exposure outlined is equivalent to that of:

    - Perform four minutes of cryotherapy treatment to left-superior pulmonary vein followed by four minutes to left-inferior pulmonary vein, right-inferior pulmonary vein and lastly, right-superior pulmonary vein. Prior to each treatment to a vein, repositioning of the catheter occurs. Finally, retraction of the cryoablation catheter into the introducer sheath, and

remain in left atrium while the physician verifies electrical potentials of all four pulmonary veins.

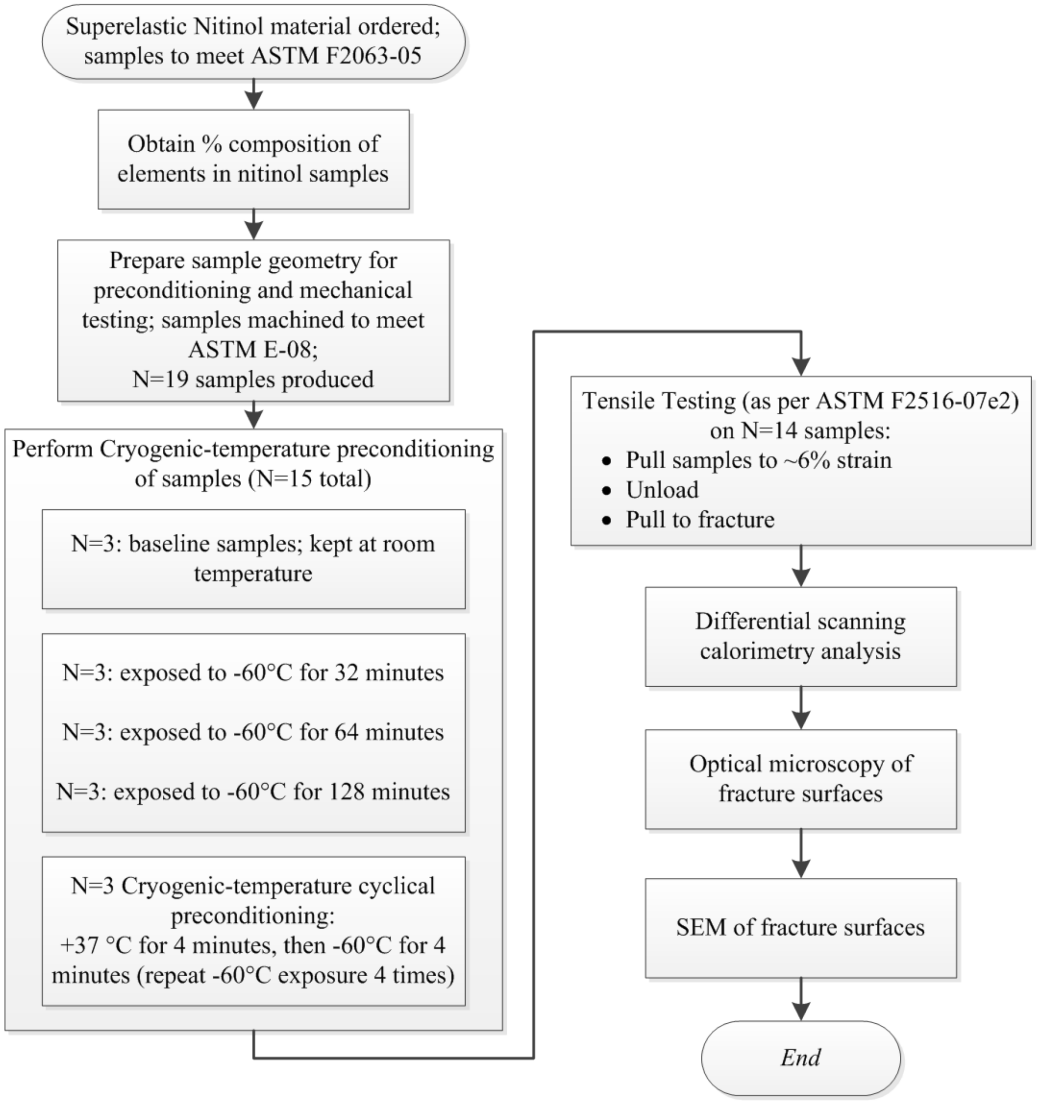

Figure 3.1 Experimental test plan Version 1.

During the handling of samples for machining after the described cryo-temperature preconditioning outlined in Figure 3.1, the traceability of all fifteen samples was unfortunately lost. All fifteen samples proceeded to be put through the aforementioned tensile testing, differential scanning calorimetry analysis, fractograph image analysis, and

scanning electron microscope analysis. Therefore, this group of samples were uniquely identified and relabeled as Original 1 through Original 15, or O1 to O15 for short, respectively.

3.2.2 Experimental Test Plan – Version 2

Flowchart 3.2 outlines an additional test plan devised for this research, created primarily to account for the loss of traceability of the previous N=15 samples. This additional testing focused primarily on establishing a correlation of mechanical properties provided through experimental test plan version 1 with respect to the equivalent preconditioning originally carried out. Furthermore, this plan also carried out a more extensive type of cryo-temperature thermal cyclical preconditioning to a subset of remaining samples. Samples utilized in experimental test plan version 2 were appropriately identified and labeled. All traceability was respected and retained throughout all handling steps. The coupon samples (N=8 total; N=2 in each of the four subgroups) were identified and labeled as Coupon A through Coupon D, or CA through CD, respectively. The remaining 2 dog-bone sheet samples were also identified and labeled accordingly as Exova Sample A and Exova Sample B, or ExovaA and ExovaB for short.

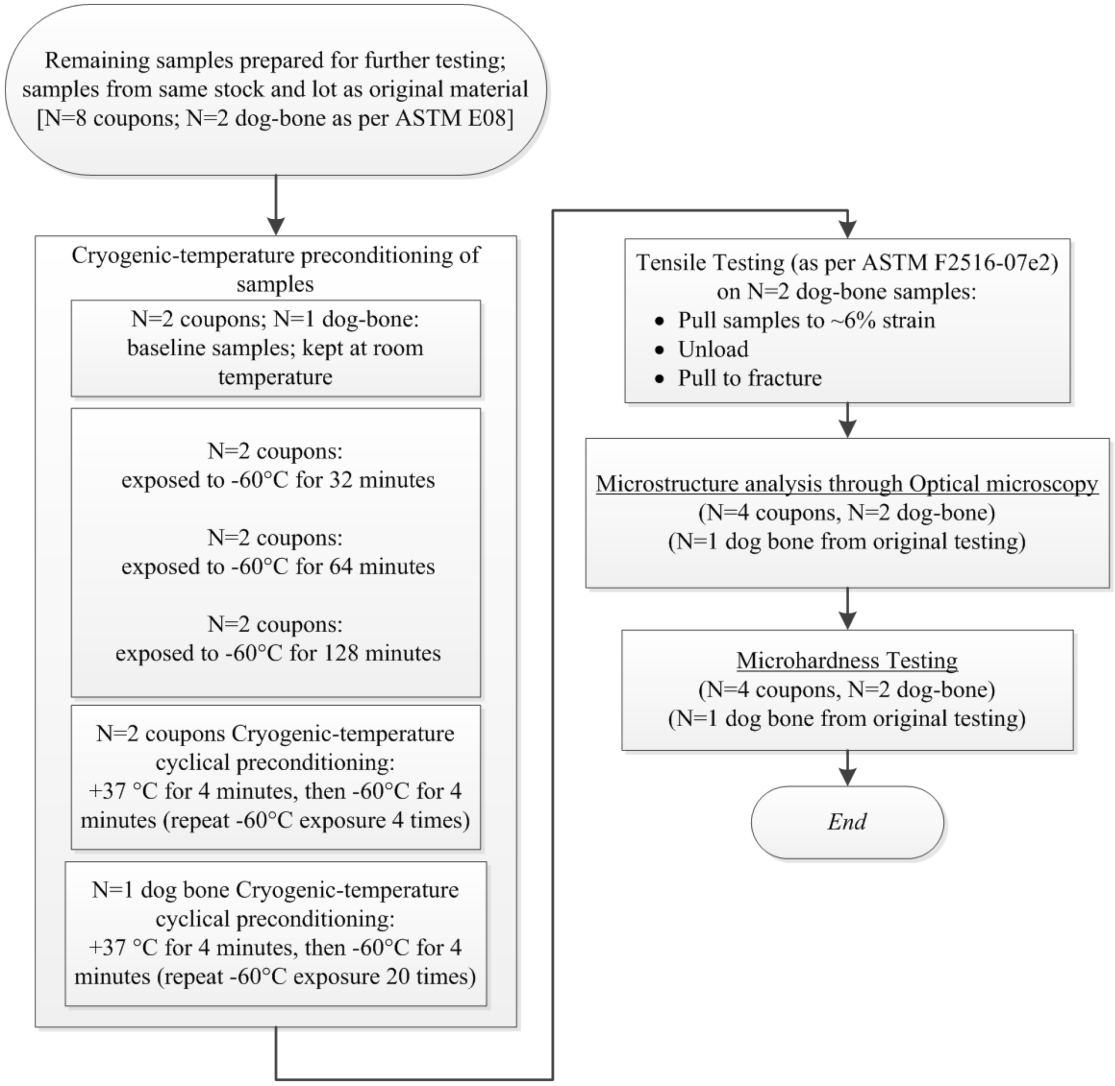

Figure 3.2 Experimental test plan Version 2.

3.3 Experimental Materials

3.3.1 Nitinol Grade SE508

The nickel-titanium alloy chosen for this study was fully annealed superelastic nitinol alloy SE508, which complies with ASTM F2063-05 Wrought Nickel-Titanium Shape Memory Alloys for Medical Devices and Surgical implants [45]. The chemical

composition is shown in Table 3.1; as can be seen, the principal alloying elements for the nitinol alloy are nickel and titanium.

Table 3.1 Composition of fully annealed superelastic nitinol alloy SE508 sheet supplied [45].

Composition Analysis (% wt)								
C	Si	Mn	P	S	Cr	Ni	Fe	Mo
0.02	/	/	/	/	0.005	55.9	0.005	/
Ti	Al	N	Cu	Co	O+N	H	Nb	
44.0482	/	/	0.005	0.005	0.0239	0.0009	0.005	

3.3.2 Sample Preparation

The superelastic nitinol alloy SE508 was supplied in the normalized conditions, as a sheet of thickness 1.0mm (Heraeus Inc.). The sheet was then machined into sheet-type tensile testing samples, as per ASTM E-08, as seen in Figure 3.3.

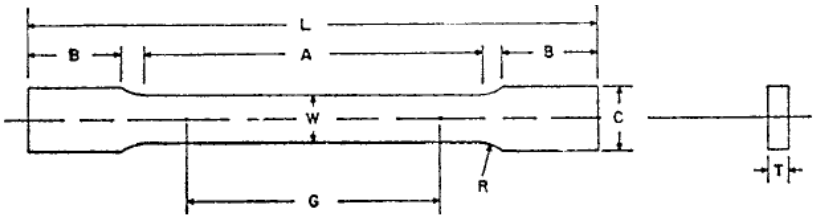

	Dimensions	
	Standard Specimens	
	Plate-Type, 40 mm [1.500 in.] Wide	Sheet-Type, 12.5 mm [0.500 in.] Wide
	mm [in.]	mm [in.]
G—Gage length (Note 1 and Note 2)	200.0 ± 0.2 [8.00 ± 0.01]	50.0 ± 0.1 [2.000 ± 0.005]
W—Width (Note 3 and Note 4)	40.0 ± 2.0 [1.500 ± 0.125, -0.250]	12.5 ± 0.2 [0.500 ± 0.010]
T—Thickness (Note 5)		thickness of material
R—Radius of fillet, min (Note 6)	25 [1]	12.5 [0.500]
L—Overall length, (Note 2, Note 7, and Note 8)	450 [18]	200 [8]
A—Length of reduced section, min	225 [9]	57 [2.25]
B—Length of grip section (Note 8)	75 [3]	50 [2]
C—Width of grip section, approximate (Note 4 and Note 9)	50 [2]	20 [0.750]

Figure 3.3 Sheet type tensile testing sample preparation, as per ASTM E-08 [46].

3.4 Cryogenic-Temperature Preconditioning

3.4.1 Cryogenic-Temperature Steady-State Treatment

Steady-state treatments outlined in experimental test plan version 1 and version 2 consists of cooling test specimens to approximately -60°C and holding them at this low temperature for different specified durations. This was carried out by submerging the specimen samples into a low-temperature isopropyl alcohol (99%) bath. The temperature of the isopropyl alcohol bath was constantly monitored by means of a thermocouple located in the liquid. The cryo-temperature treatment schedule is summarized in Table 3.2 below.

Table 3.2 Steady-state cryogenic-temperature treatment schedule for test samples.

Steady-State Temperature Treatment
-60°C for a duration of 32 minutes
-60°C for a duration of 64 minutes
-60°C for a duration of 128 minutes

Figure 3.4 Multi-Cool Low-Temperature bath.

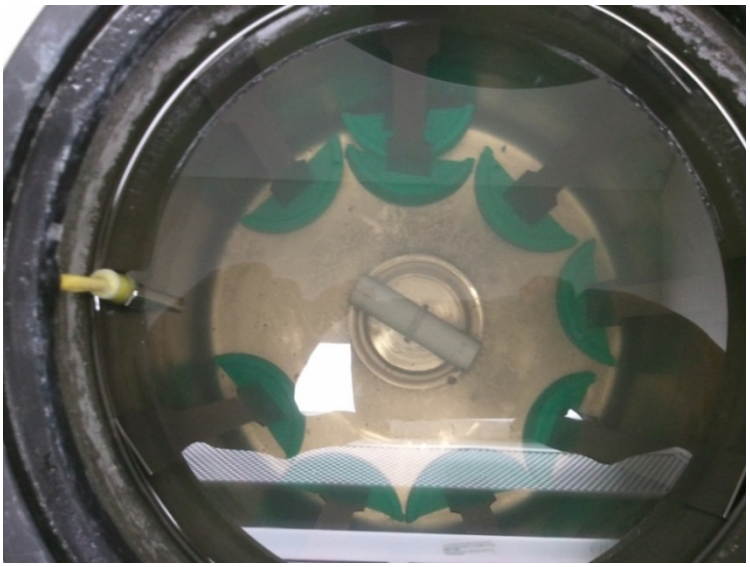

Figure 3.5 Samples submerged in isopropyl alcohol 99% cryo bath.

3.4.2 Cryogenic-Temperature Cyclical Treatment

Cyclical treatments consist of first exposing the test specimens to a controlled water bath at an approximate regulated temperature of +37°C for a duration of four minutes. This was carried out by submerging the specimen samples into warmed water bath. The temperature of the water bath was constantly maintained by means of a thermal circulating water pump. Thereafter, the specimens were transferred from the water to the isopropyl alcohol bath, cooling the specimens to approximately -60°C and holding at this low temperature for four minutes. Thereafter, the process is repeated, carefully transferring the test specimens from one bath to the other. The cyclical cryo-temperature treatment schedule is summarized in Table 3.3 and 3.4.

Table 3.3 Cyclical cryogenic-temperature treatment schedule for N=3 test samples in test plan version 1.

Cycle	Temperature Treatment
1	+37°C for 4 minutes
	-60°C for 4 minutes
2	+37°C for 4 minutes
	-60°C for 4 minutes
3	+37°C for 4 minutes
	-60°C for 4 minutes
4	+37°C for 4 minutes
	-60°C for 4 minutes

Table 3.4 Cyclical cryogenic-temperature treatment schedule for N=1 test sample in test plan version 2.

Cycle	Temperature Treatment
1	+37°C for 4 minutes
	-60°C for 4 minutes
2	+37°C for 4 minutes
	-60°C for 4 minutes
3	+37°C for 4 minutes
	-60°C for 4 minutes
4	+37°C for 4 minutes
	-60°C for 4 minutes
5	+37°C for 4 minutes
	-60°C for 4 minutes
6	+37°C for 4 minutes
	-60°C for 4 minutes
7	+37°C for 4 minutes
	-60°C for 4 minutes
8	+37°C for 4 minutes
	-60°C for 4 minutes
9	+37°C for 4 minutes
	-60°C for 4 minutes
10	+37°C for 4 minutes
	-60°C for 4 minutes
11	+37°C for 4 minutes
	-60°C for 4 minutes
12	+37°C for 4 minutes
	-60°C for 4 minutes
13	+37°C for 4 minutes
	-60°C for 4 minutes
14	+37°C for 4 minutes
	-60°C for 4 minutes
15	+37°C for 4 minutes
	-60°C for 4 minutes
16	+37°C for 4 minutes
	-60°C for 4 minutes
17	+37°C for 4 minutes
	-60°C for 4 minutes
18	+37°C for 4 minutes
	-60°C for 4 minutes
19	+37°C for 4 minutes
	-60°C for 4 minutes
20	+37°C for 4 minutes
	-60°C for 4 minutes

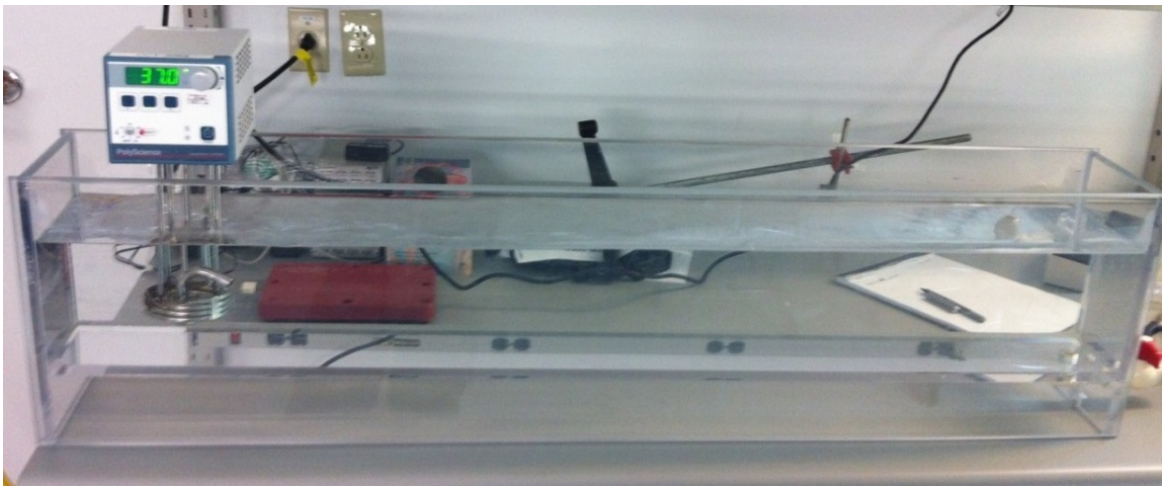

Figure 3.6 Warm water bath with thermal circulating water pump.

3.5 Material Properties Testing

3.5.1 Mechanical Tensile Testing

During experimental test plan versions 1 and 2, mechanical tensile testing was performed on a MTS RT10 Alliance test frame outfitted with a 10kN load cell and heavy duty mechanical wedge grips. Samples were pulled at a stroke rate of 0.00320 mm/s.

3.5.2 Microhardness Testing

Microhardness measurements were determined using a Mitutoyo MVK-H1 Micro-Vickers Hardness Tester, using 1000gf load settings.

3.6 Fracture Surface Analysis

3.6.1 Digital Microscope

The fracture surfaces of the tensile tested samples from experimental test plan version 1 were initially examined using a digital microscope (Keyence VHX-2000) that operates from 0.1x to 5,000x magnification range, and offers 2D/3D imaging reconstruction capabilities. Micrographs from fracture samples were three-dimensionally stacked and stitched (by the software) to assemble and render composite images of the fracture surfaces.

3.6.2 Scanning Electron Microscope

The fracture surfaces, which were cleaned ultrasonically in an ethanol bath, were examined using a JEOL JSM-5900 low vacuum scanning electron microscope that operates at a resolution of up to 3 nm at a voltage of 30kV.

3.7 Material Microstructure Analysis

3.7.1 Scanning Electron Microscope

Examination surfaces of test samples were prepared by chemical etching to reveal the microstructure (etchant: 3.2% HF, 14.6% HNO_3, balance deionized water) [47]. They were then further examined using the Hitachi S-3400N scanning electron microscope.

3.7.2 X-Ray Diffraction

Examination of samples ExovaA (baseline) and ExovaB (20 cryo-cycles) were investigated in order to determine and identify microstructure phases. A Panalytical X-Ray Powder Diffraction X'pert Pro Machine was used to perform the analysis.

3.8 Material Thermoanalytical Analysis

3.8.1 Differential Scanning Calorimetry

Because traceability was questioned for the first original 15 samples tested, those original samples underwent a DSC analysis. The differential scanning calorimeter used was the TA Discovery DSC.

CHAPTER 4

4.1 Results and Discussions

4.1.1 Overview

In this chapter, the results of the experiments described in Chapter 3 are presented and discussed with references to the literature review in Chapter 2. In this work, fully annealed superelastic nitinol alloy, which complies with ASTM F2063-05 Wrought Nickel-Titanium Shape Memory Alloys for Medical Devices and Surgical implants, has been studied. In the following sections, the effect on the mechanical properties of the studied nitinol, such as tensile testing and hardness, are presented. In each section, the aim is to compare the effects of cryogenic-temperature treatment with respect to the baseline control samples. Following this, both fracture surface and scanning electron microscope microscopy images were taken for specific samples with the aim again, to compare the effects of cryogenic-temperature treatment with respect to the baseline control samples. Lastly, differential scanning calorimetry results will be discussed for the original 15 samples.

Table 4.1 below outlines sample identification and cryo-temperature conditioning treatment of all samples being discussed.

Table 4.1 Cryogenic-temperature conditioning with sample identification.

Sample Identification	Cryo-Temperature Conditioning Received
*Samples 1 through 15	N=3: baseline samples; no conditioning.
	N=3: -60°C for a duration of 32 minutes.
	N=3: -60°C for a duration of 64 minutes.
	N=3: -60°C for a duration of 128 minutes.
	N=3: cyclical treatment of +37°C for 4 minutes followed by -60°C for 4 minutes. Total treatment time was 32 minutes.
Coupon A [32min_-60C] (1 cryo-cycle)	N=2: -60°C for a duration of 32 minutes.
Coupon B [64min_-60C] (1 cryo-cycle)	N=2: -60°C for a duration of 64 minutes.
Coupon C [128min_-60C] (1 cryo-cycle)	N=2: -60°C for a duration of 128 minutes.
Coupon D [32min_cyc] (4 cryo-cycles)	N=2: +37°C for 4 minutes followed by -60°C for 4 minutes. Total treatment time was 32 minutes.
Exova A [Baseline] (0 cryo-cycles)	N=1: baseline samples; no conditioning.
Exova B [160min_cyc] (20 cryo-cycles)	N=1: cyclical treatment of +37°C for 4 minutes followed by -60°C for 4 minutes. Total treatment time was 160 minutes.

**Note: as described in Chapter 3, all traceability for original samples identified 1 through 15 was lost during initial mechanical testing.*

4.2 Material Thermoanalytical Investigation

4.2.1 Differential Scanning Calorimetry

Because traceability was lost for the first original 15 samples tested (reference section 3.2.1), those original samples underwent differential scanning calorimetry analysis. The main purpose was to ensure that transformation temperatures for all samples did not change given the different cryogenic temperature treatments.

Sample were first cut with a micro-cut diamond saw using a very low feed rate (0.005 inches/min), constantly flushed with deionized water during cutting to avoid sample heating, and then were followed by three minutes of ultrasonic cleaning in iso-propyl alcohol (IPA), followed by three minutes in deionized water. The samples were then air dried for 24 hours before utilizing the differential scanning calorimeter. Figure 4.1 outlines all DSC thermograph curves obtained for each of the original 15 samples.

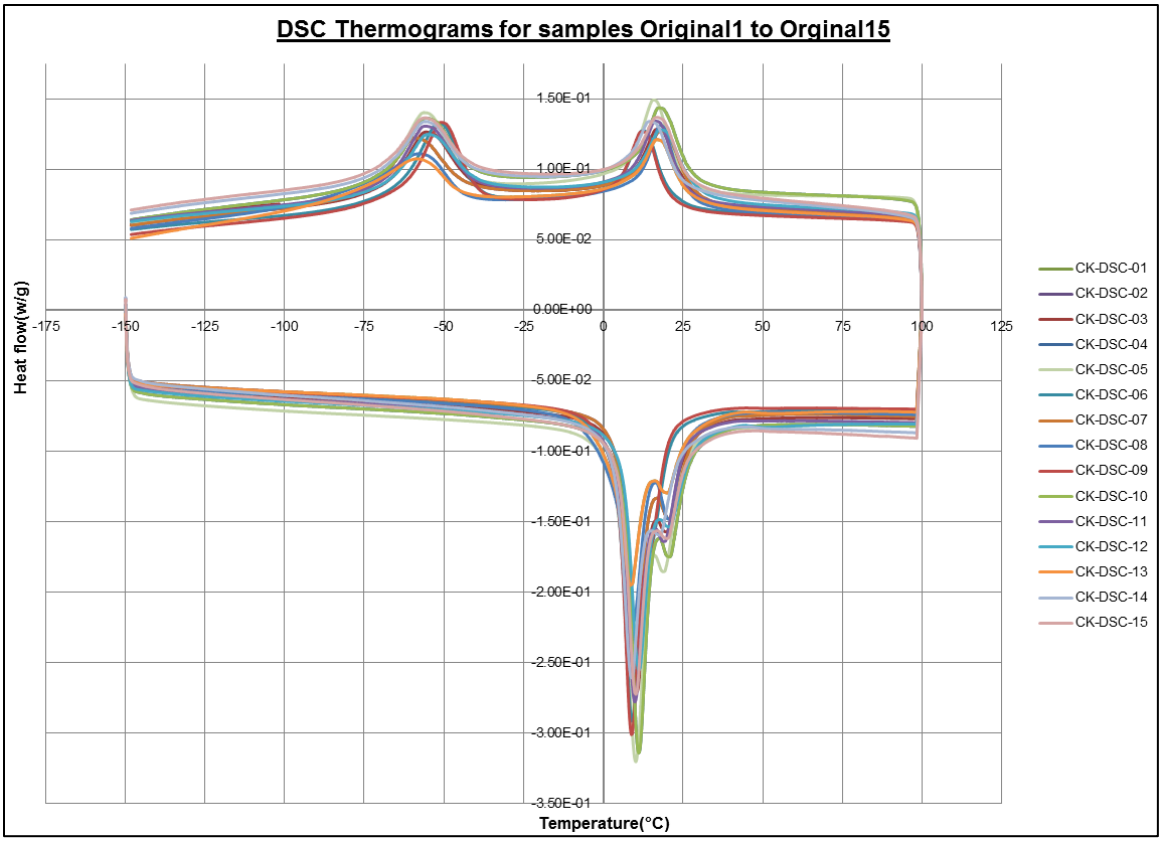

Figure 4.1 Differential scanning calorimeter curves produced for the original 15 samples that lost traceability.

From Figure 4.1, we can see four differentiable peaks in the curve: martensite peak at approximately -55°C, martensite to R-phase peak at approximately 10°C, austenite peak at approximately 16°C, and an austenite to R-phase peak at approximately 18°C. As can be observed, using the tangent method from ASTM 2004-05 [48], transformation temperature peaks and their respective transformation temperatures M_s, M_f, R_s, R_f, A_s, and A_f, can be deemed equivalent. Approximated extrapolated transformation temperatures are captured in Table 4.2.

Table 4.2 Approximated extrapolated transformation temperatures.

Transformation temperatures	Samples							
	01	02	03	04	05	06	07	08
As	5.0	5.2	5.5	6.1	5.4	5.9	5.0	5.5
Af	25.3	24.7	26.9	27.6	26.0	24.7	27.8	26.4
Rs	27.2	24.1	27.6	28.1	24.7	25.3	29.0	26.5
Rf	7.6	6.8	9.0	9.6	8.4	6.6	9.6	9.2
Ms	-43.5	-40.6	-41.4	-41.9	-42.7	-40.3	-44.0	-43.7
Mf	-69.3	-68.9	-68.7	-68.6	-68.0	-69.5	-71.0	-73.7

Transformation temperatures	Samples							Avg Temps
	09	10	11	12	13	14	15	
As	5.8	5.4	5.8	6.0	5.7	5.8	5.2	5.6
Af	24.1	24.9	26.0	28.0	26.9	24.6	27.0	26.1
Rs	24.9	26.0	25.9	28.9	26.8	24.4	27.5	26.5
Rf	7.6	6.1	7.6	9.0	8.8	6.8	7.9	8.0
Ms	-41.7	-42.6	-41.4	-40.2	-44.2	-42.6	-42.2	-42.2
Mf	-70.5	-68.3	-69.0	-68.8	-72.1	-69.4	-69.8	-69.7

Because of the aforementioned typical clinical use case conditions and chosen temperature cycling profile for clinical applications, it is important to observe that the martensite transformation peak occurs around the -55°C mark, which coincides with the lower temperature cycle of -60°C.With respect to M_s, M_f, A_s, and A_f, Figure 4.2 plots respectively the clinical temperature conditions with respect to the average transformation temperatures observed. This overlap between the clinical use conditions and the transformation temperatures may result in some property changes that affect the use of this material.

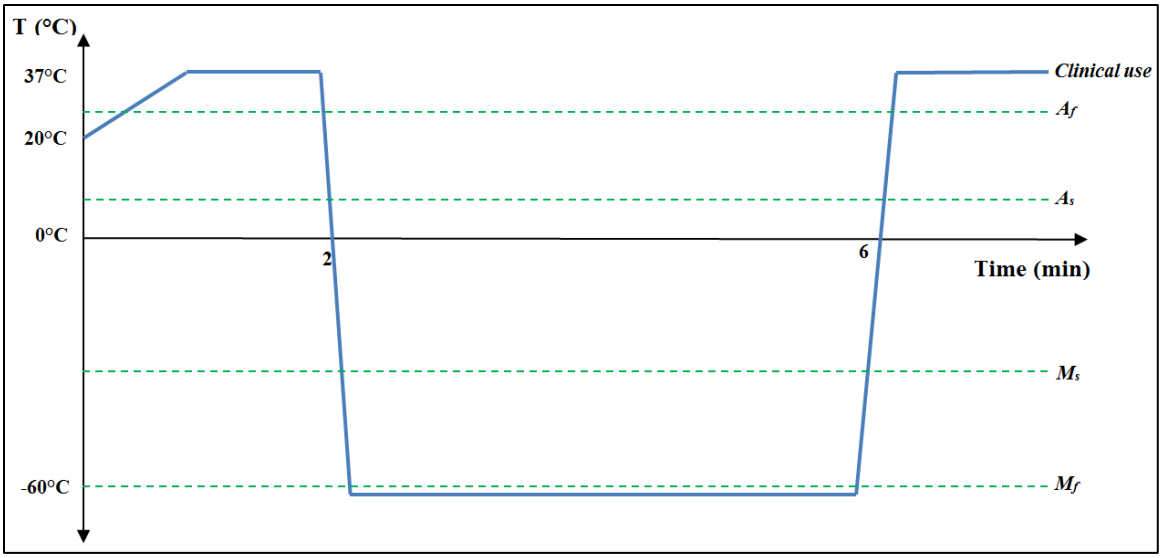

Figure 4.2 Average martensite and austenite transformation temperatures with respect to clinical use temperature profile.

4.3 Materials Properties Testing

4.3.1 X-Ray Diffraction

Diffraction patterns for samples ExovaA (baseline) and ExovaB (20 cryo-cycles) are noted in Figures 4.3 and 4.4 below. It should be noted that for sample ExovaA, the martensite and austenite percentage are 62.3% and 37.7%, respectively. For ExovaB (20 cryo-cycles), the martensite and austenite percentage are 36% and 64%, respectively. This change in relative percentage of each respective constituent is hypothesized to have an effect on the material's mechanical properties and will be examined further.

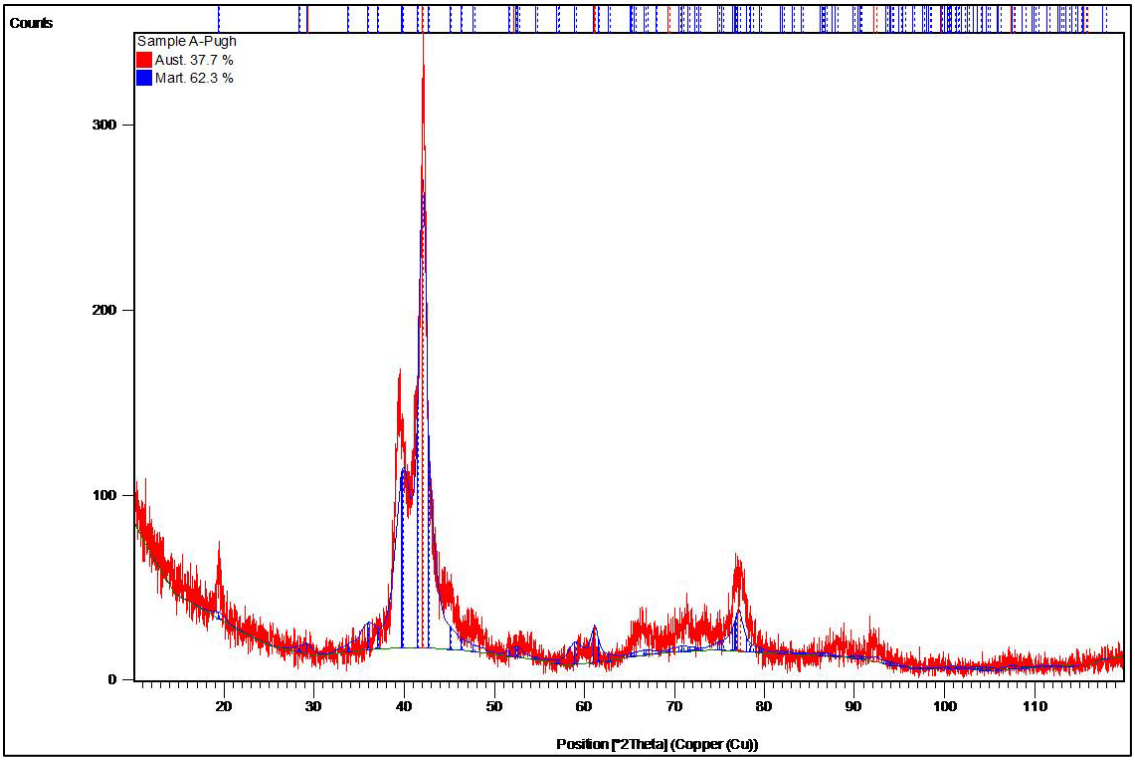

Figure 4.3 XRD pattern for sample ExovaA (baseline).

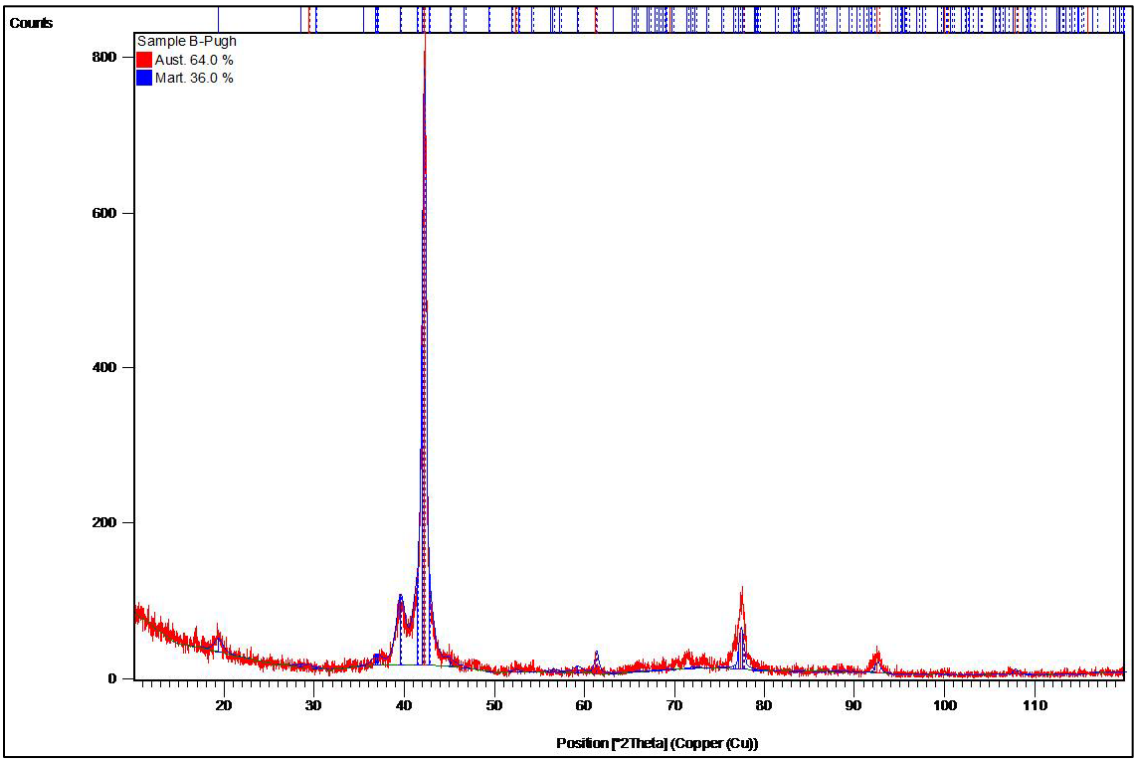

Figure 4.4 XRD pattern for sample ExovaB (20 cryo-cycles).

4.3.2 Mechanical Tensile Testing

Figure 4.5 shows the stress-strain curves for samples 2 through 15, and Exova A and B, all obtained through tensile testing each sample. Figure 4.6 shows the stress-strain hysteresis loops of each respective curve.

It should be noted that sample 1 of the group was used to calibrate the tensile testing apparatus and therefore no data was produced for it. As observed, all samples did exhibit typical stress-strain behavior to that of shape memory alloys in particular, nickel-titanium alloys. Additionally, hysteresis memory loops are present in all samples, and curves do vary in a typical manner again to that of nitinol material.

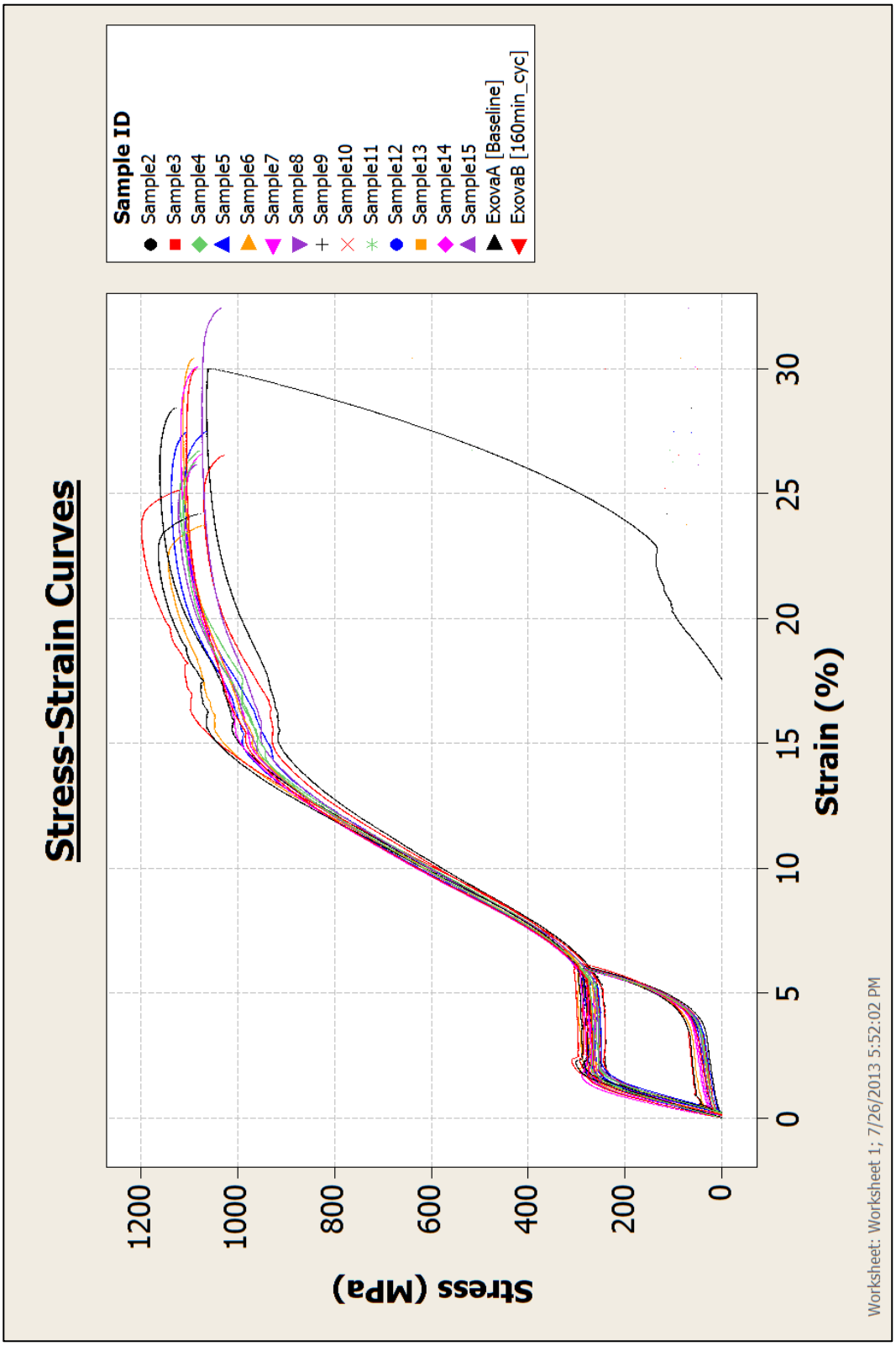

Figure 4.5 Stress-strain curve results for all samples tensile tested (samples 2 through 15; Exova A and Exova B).

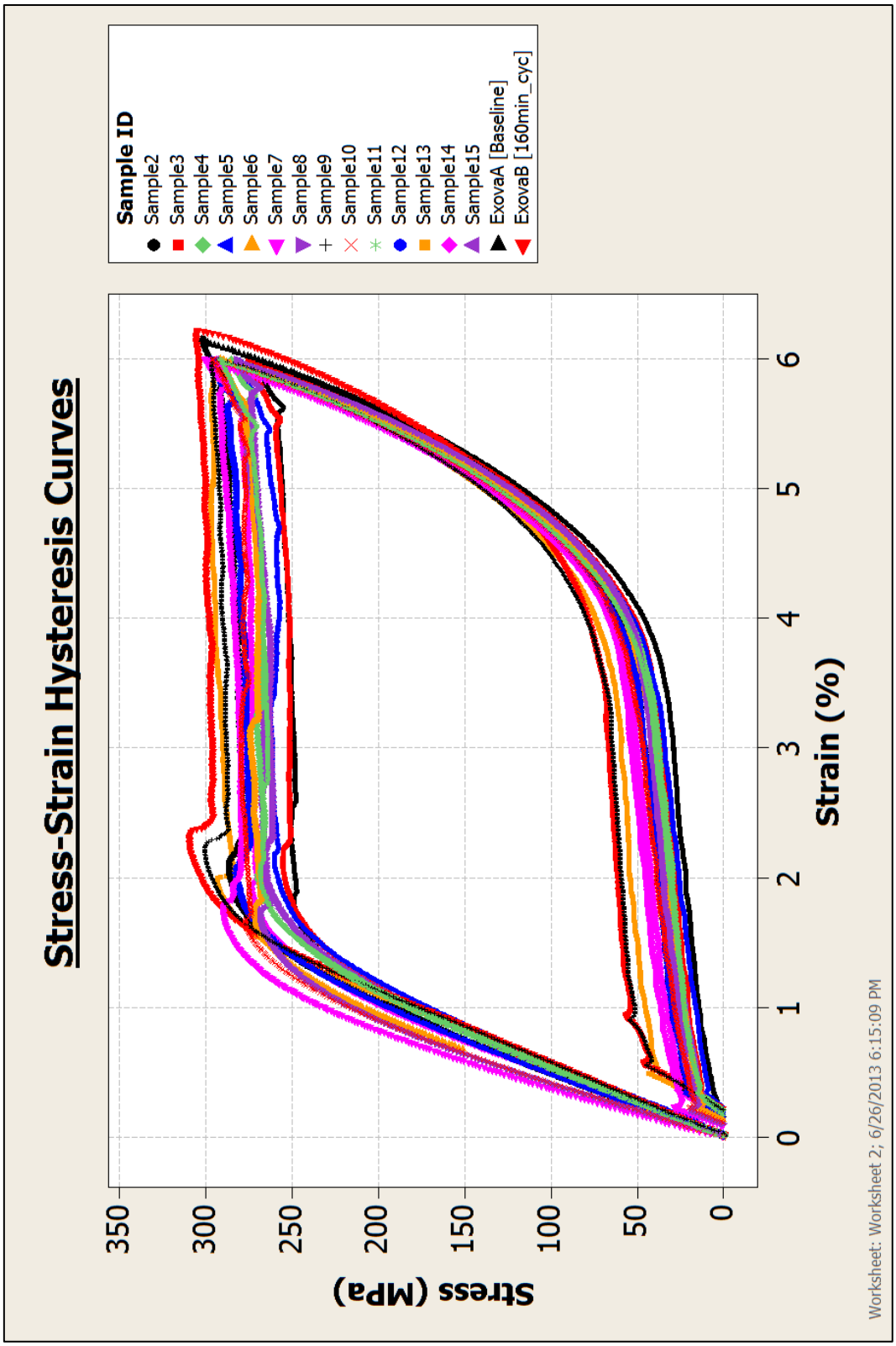

Figure 4.6 Stress-strain hysteresis curve results for all samples tensile tested (samples 2 through 15; Exova A and Exova B).

The variation present in all curves can be concluded to be typical of Nitinol [3,4,5], especially given the inherent shape memory and superelasticity properties of the material. However, slight differences can be observed when investigating specific aspects of each curve and their respective mechanical properties. When examining the data produced for samples 2 through 15, it is hypothesized that there does exist a 'subgroup' of data that lies outside of the population of stress-strain curves; those are believed to belong to samples that have been exposed to multiple cyclical cryo-temperature treatments (i.e., $+37^{o}C$ for 4 minutes followed by 4 minutes at $-60^{o}C$, repeated 4 times). This was further complemented when tabulating extracted mechanical properties from the stress-strain data. Table 4.3 below summarizes key mechanical properties for all samples tensile tested.

Table 4.3 Mechanical properties extracted from stress-strain curves.

Sample	~ Final Yield Strength	~ Yield Strength, Aust, cyc 1	~ Yield Strength, Aust, cyc 2	Tensile Strength	LPS, at 2.5%	UPS, at 3%, cyc 1	UPS, at 3%, cyc 2	ΔUPS	ΔPS
	(MPa)	(MPa)	(MPa)	(MPa)	(MPa)	(MPa)	(MPa)	(MPa)	(MPa)
2	927.77	248.14	239.92	1064.99	26.54	249.61	239.41	10.19	223.07
3	929.21	254.52	240.35	1070.81	31.78	251.54	241.19	10.35	219.76
4	959.91	270.11	254.03	1120.27	34.00	269.47	258.05	11.42	235.47
5	990.70	282.20	267.46	1137.69	41.25	275.89	264.96	10.94	234.64
6	970.54	268.76	258.84	1113.30	36.44	273.81	262.04	11.77	237.37
7	980.24	280.45	272.25	1117.99	49.01	280.23	270.39	9.83	231.22
8	950.50	265.11	255.30	1074.60	38.58	263.27	255.01	8.27	224.69
10	983.72	275.93	263.85	1104.46	42.91	279.84	267.65	12.19	236.93
11	942.72	268.71	251.93	1113.00	34.93	264.62	252.80	11.81	229.69
12	929.16	258.79	243.78	1109.57	29.81	261.91	249.39	12.52	232.10
14	974.64	270.24	262.33	1107.30	46.13	275.68	264.40	11.28	229.54
15	961.79	265.16	249.37	1123.07	36.09	266.59	254.39	12.20	230.50
9	1064.18	296.88	281.11	1164.47	61.74	288.23	276.63	11.61	226.49
13	1047.75	291.79	274.81	1144.18	55.87	290.64	279.33	11.31	234.78
ExovaA [baseline] (0 cryo-cycles)	986.84	254.71	241.28	1161.30	41.54	279.98	268.82	11.15	238.43
ExovaB [160min_cyc] (20 cryo-cycles)	1085.39	287.06	270.22	1199.16	63.84	296.31	285.06	11.25	232.47

When examining the original sample set, specimens 2 through 15, the cryogenic-temperature conditioning the samples received, excluding samples 9 and 13, are postulated to have had no significant effect on the material and its respective mechanical properties. However, it is hypothesized that the multiple cycle cryogenic-temperature treatment, was performed on both samples 9 and 13 and that this cyclic treatment is responsible for the effect on both the samples respective tensile strength, estimated final elastic yield strength, and the overall ductility of the sample, respectively, and will be

examined further. Figure 4.7 and 4.8 represent stress-strain curves for the hypothesized groupings of the original 15 samples previously described.

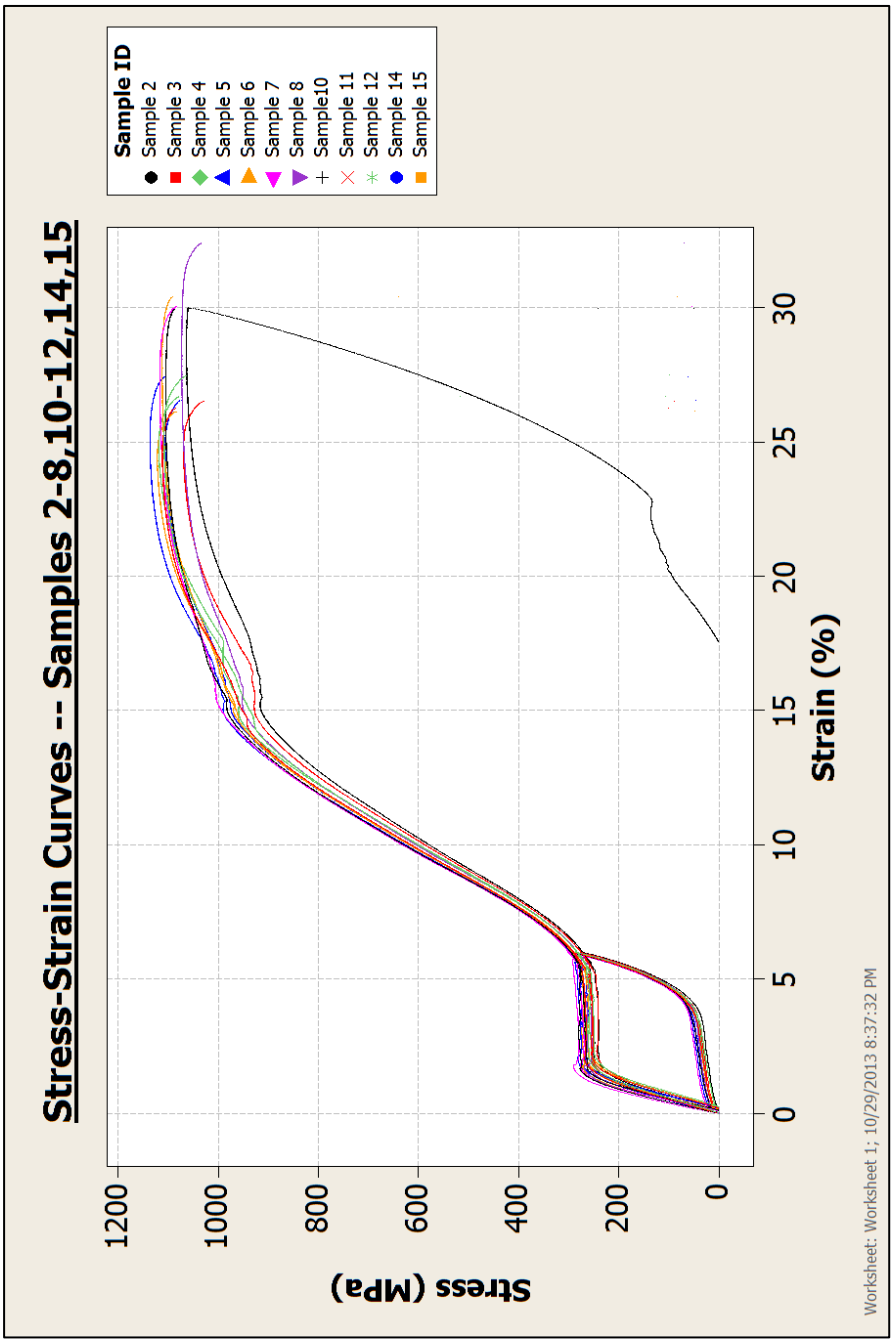

Figure 4.7 Stress-strain curve results for samples 2-8, 10-12, 14, and 15.

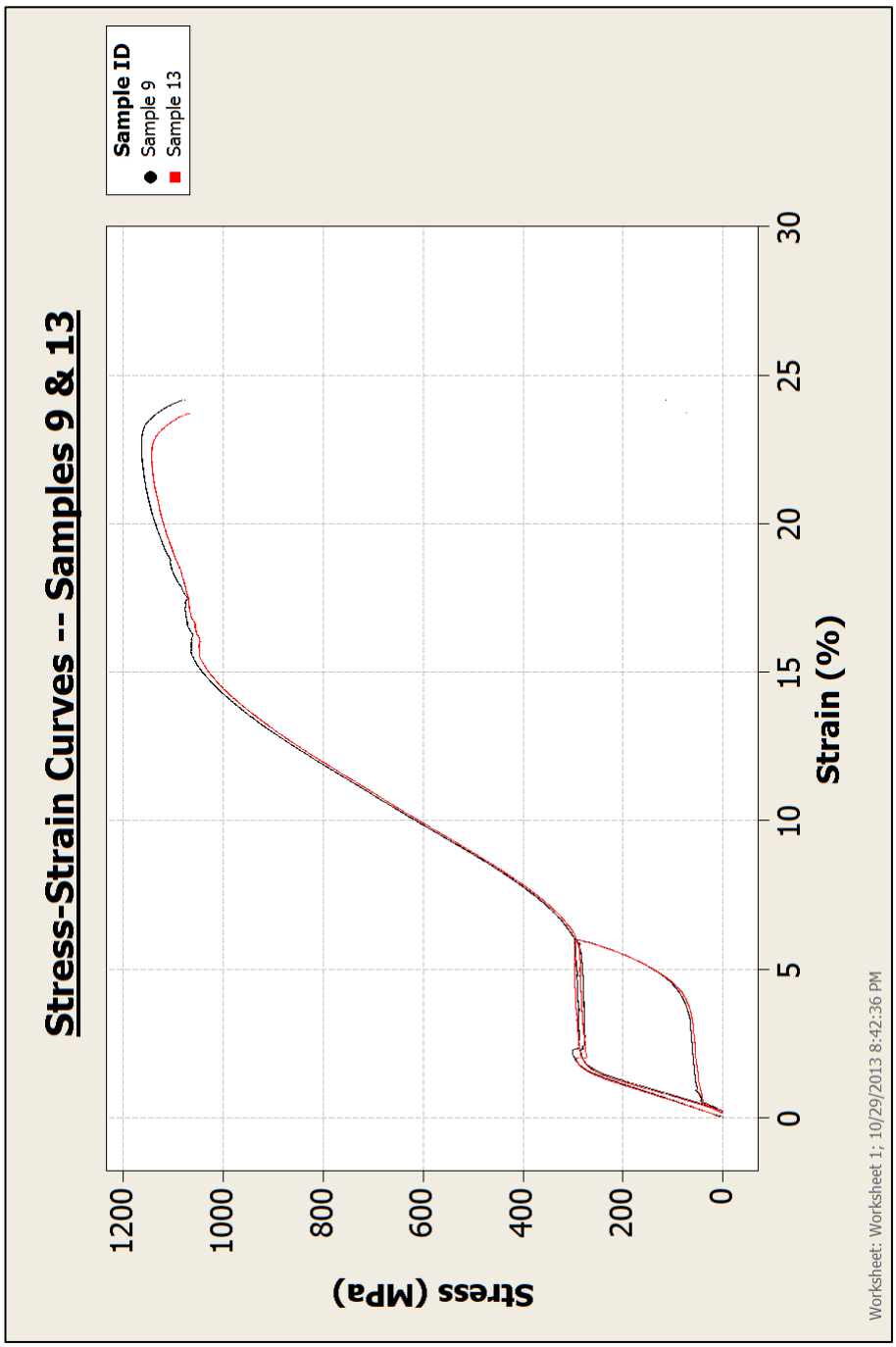

Figure 4.8 Stress-strain curve results for samples 9 and 13.

If one moves forward holding this hypothesis, the current data set could be examined as follows: samples 2-8, 10-12, 14 and 15 all display typical properties to that of nitinol, and as noted earlier, all have lost traceability. It can be surmised that samples 2-8, 10-12, 14

and 15 are equivalent to sample ExovaA – (a known sample acting as a baseline; non-conditioned as per Table 4.1), and as can be observed from both Figures 4.5 and 4.6 as well as sample ExovaA's respective mechanical properties listed in Table 4.3, which lists comparable mechanical properties as the aforementioned sample sets. Since traceability remains for sample ExovaA, it will act as the new baseline sample for both cryo and non-cryo treated samples, excluding samples that have received multiple cyclical cryogenic-temperature treatments. Sample 9 from the original 15 sample data set, one of two samples previously hypothesized to be in a subgroup outside of the general sample population, will represent a cyclical cryogenic-temperature treated sample. Lastly, to confirm this hypothesis and further the analysis, sample ExovaB will now be included, which was added following experimental test plan version 2 (previously described in Chapter 3) to support the hypothesis that cyclical cryogenic-temperature treatments do, in fact, have some kind of effect on the material's mechanical properties. Figure 4.9 replots the stress-strain curves for Sample 9, ExovaA and ExovaB, respectively and it is apparent that Exova B and Sample 9 show significant similarities.

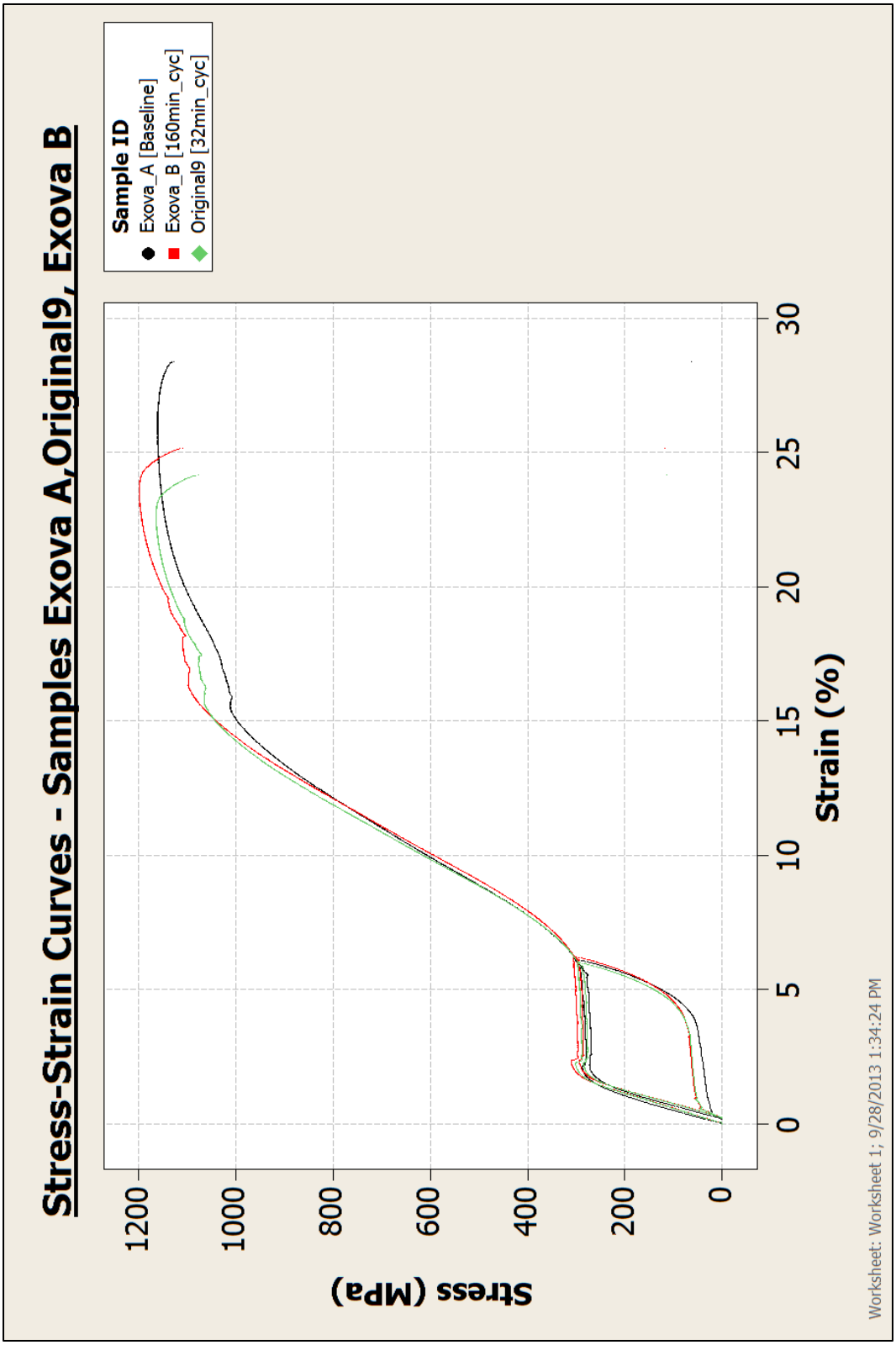

Figure 4.9 Stress-strain curve results for samples Exova A, Sample 9 and Exova B.

Table 4.4 summarizes mechanical properties for Sample 9, ExovaA and ExovaB with respect to key mechanical properties of interest.

Table 4.4 Specific mechanical properties for samples 9, Exova A, and Exova B.

Sample	~ Final Yield Strength (MPa)	LPS, at 2.5% (MPa)	UPS, at 3%, cyc 1 (MPa)	ΔPS (MPa)	Tensile Strength (MPa)
Exova A [baseline] (0 cryo-cycles)	986.8	41.5	280.0	238.4	1161.3
Original9 [32min_cyc] (4 cryo-cycles)	1064.2	61.7	288.2	226.5	1164.5
Exova B [160min_cyc] (20 cryo-cycles)	1085.4	63.8	296.3	232.5	1199.2

Recalling that Sample 9 is assumed to have received four cycles of cryogenic-temperature treatments for a total duration of 32 minutes, and sample Exova B received 20 cycles of cryogenic-temperature treatments for a total duration of 160 minutes, a relationship can be postulated based on both the stress-strain curves produced, and the respective resulting mechanical properties. In order to further solidify our hypothesis, hardness testing was carried out on specific sample sets, and analyzed further.

4.3.3 Hardness Testing

Figure 4.10 shows the Micro-Vickers hardness values obtained. In order to respect the loss of traceability of the original set of samples 2 through 15, testing was carried out on the couponed samples – Coupon A, B, C and D, (A, B, C which had undergone

treatments as listed in Table 4.1; D which had undergone treatments as listed in Table 4.2) and these can be seen as providing mirrored data to that of samples 2 through 15, excluding sample 9. Additionally, samples ExovaA, ExovaB and sample 9 were included for comparison purposes. Recall that all samples and their respective cryogenic treatments are listed in Table 4.1.

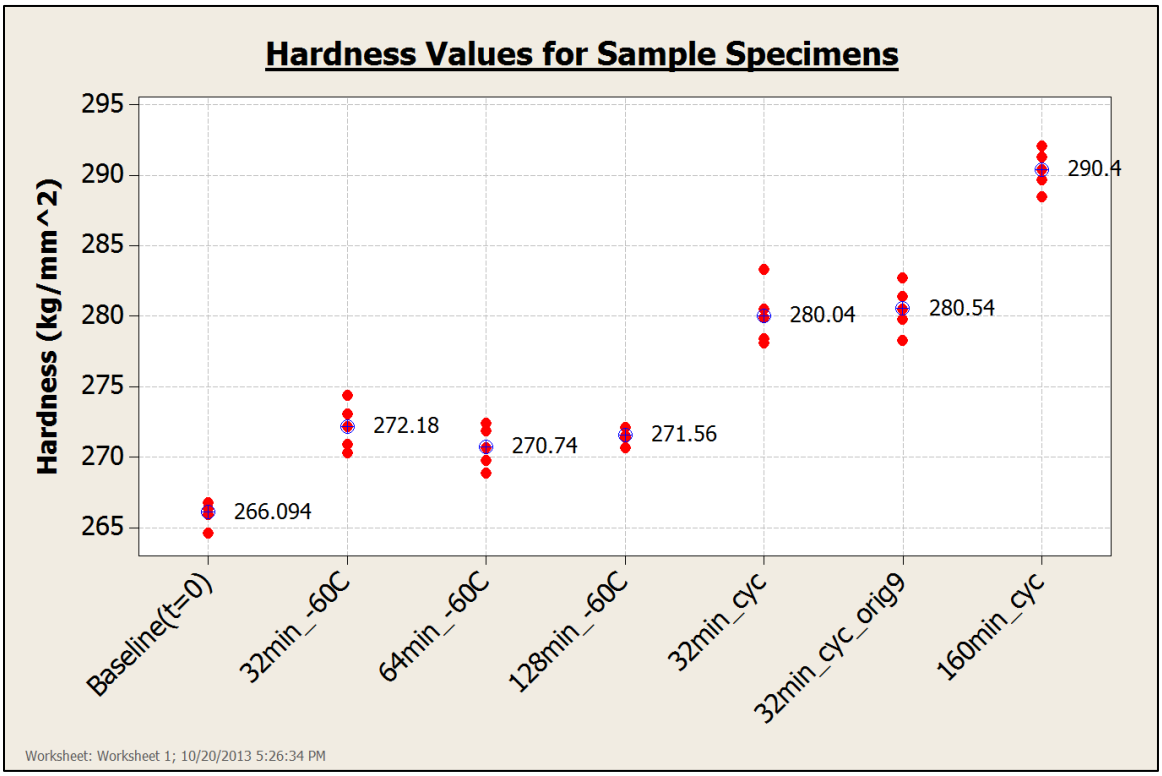

Figure 4.10 Hardness values for sample specimens.

It can be observed that Coupons A through C, all which have been exposed to different cryogenic-temperature treatment durations, at the same -60°C temperature, result in equivalent average hardness values. All these coupons only had one cryo-temperature cycle and will thus be grouped together and labeled as "One cycle_-60C". Similarly, sample 9 (32min_cyc_orig9) and Coupon D (32min_cyc) also resulted in comparable average hardness values; Coupon D will be used moving forward labeled as "4 Cycles_-

60C" since its respective traceability is confirmable and hardness values equivalent. It is clear that different hardness values are observed for samples ExovaA ("baseline") and Exova B ("20 Cycles_-60C), as originally surmised. Replotting and comparing the average hardness values as such is depicted in Figure 4.11.

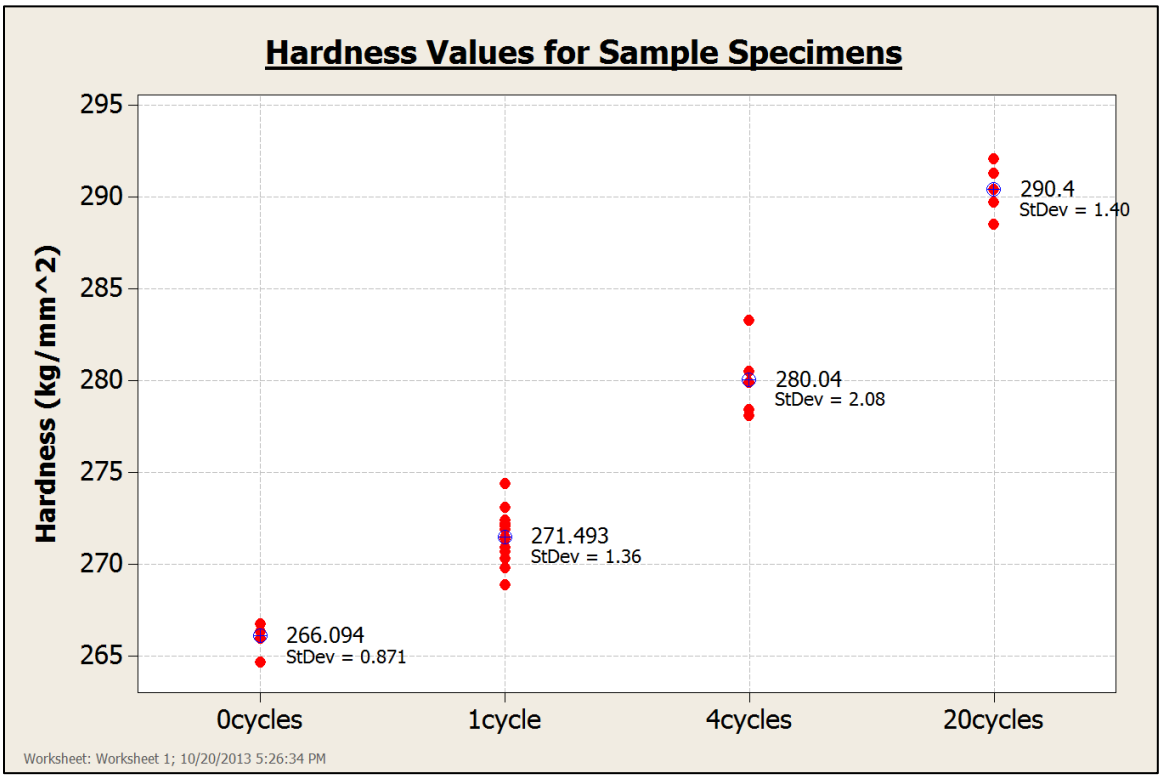

Figure 4.11 Replotted hardness values for specimens that have received increasing numbers of cryo-temperature cycles.

Due to the exhibited increase in average microhardness values for sample ExovaB, it is clear that this must be related to the increase in the number of cryogenic-temperature treatment cycles that ExovaB received with respect to the remaining population of samples. This is further summarized in Figures 4.12 and Figure 4.13. Figure 4.12 shows the hardness values for samples Coupon A through C, comparing them to the baseline sample ExovaA with respect to time. Recall that these samples were exposed to a one

cycle at a steady temperature of -60°C for different durations. It is clear from Figure 4.12 that the exposure to the low temperature has affected the hardness of the Nitinol: the average hardness has increased by approximately 5 kg/mm^2 for those samples which have been cryo-treated. It is also apparent that increasing the dwell-time at low temperatures from 32 minutes to 128 minutes has little to no effect on hardness values.

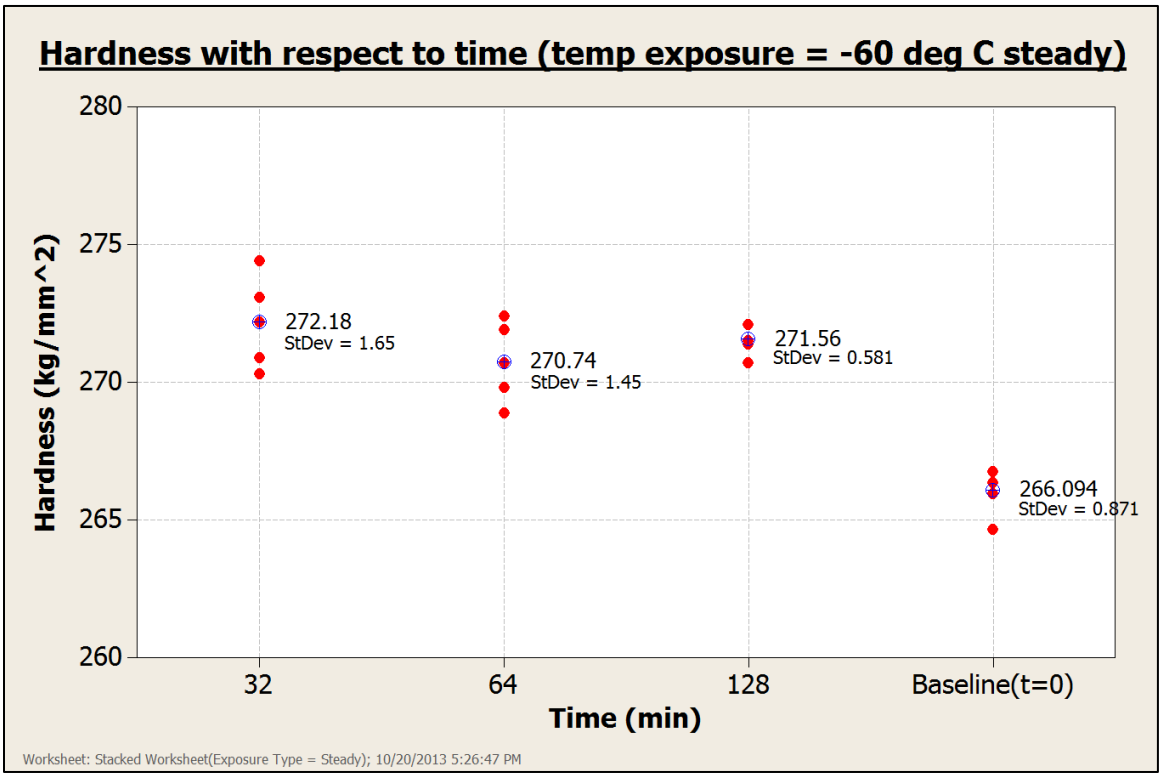

Figure 4.12 Hardness values for one-cycle cryo temperature treated samples versus untreated sample.

Figure 4.13 compares the hardness values for Coupon D (4 cycles), sample 9 (assumed 4 cycles) and ExovaB (20 cycles), all having been exposed to varying numbers of cyclical cryogenic-temperature treatments, with ExovaA which had no thermal cycling.

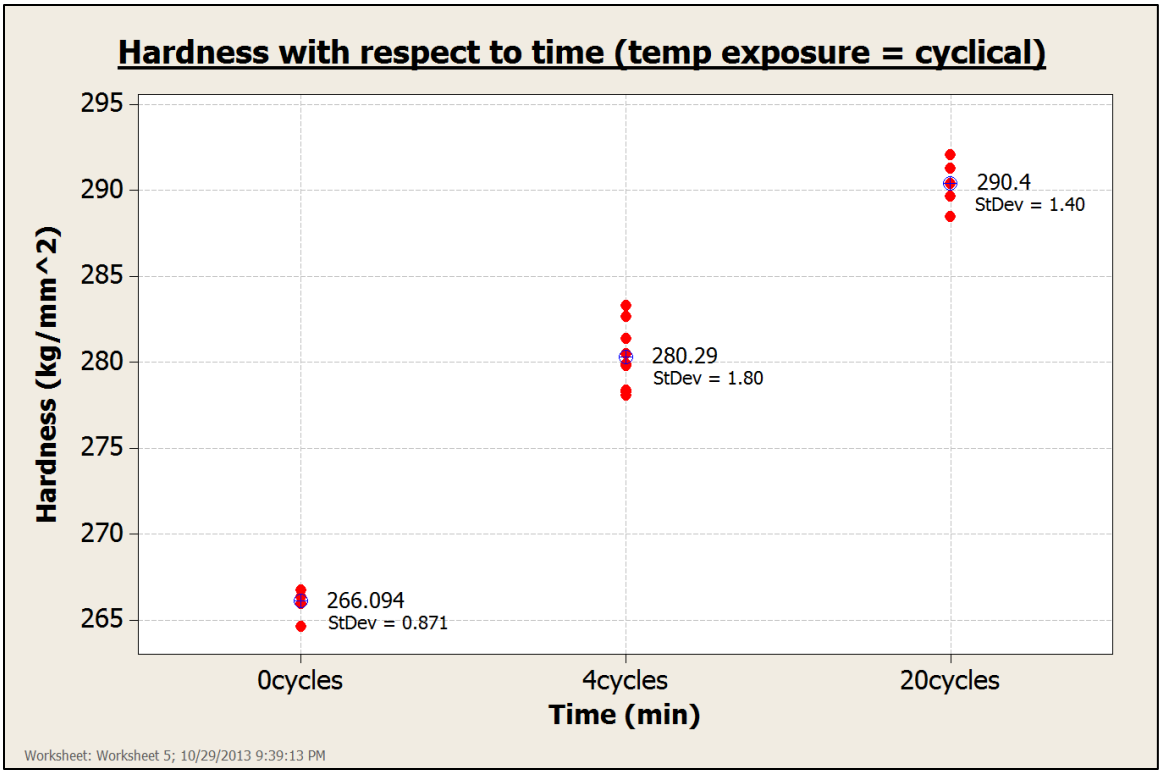

Figure 4.13 Hardness values for cyclical cryo-temperature treated samples compared to untreated material.

From Figure 4.12, we observe a slight increase in hardness for samples exposed to steady cryogenic-temperature treatments when compared to the baseline material. However, when comparing the average hardness values in both Figures 4.12 and 4.13, it is clear that samples exposed to more cycles of the cryogenic-temperature treatment show higher increases in hardness, with the hardness increasing from 266.1 kg/mm^2 for untreated material to 280 kg/mm^2 for the samples cycled 4 times, and ultimately to 290.4 kg/mm^2 for the sample cycled 20 times.

This observed change in hardness during thermal cycling, as well as the aforementioned increases in overall estimated final yield strength and tensile strengths, is thought to be

due to the fact that in this alloy, the transformation from austenite to martensite is not completely thermoelastic; that is, the accommodation strain in the parent phase is not purely elastic and there is some plastic strain. If there is some plastic deformation during the transformation from austenite (higher temperature) to martensite (at lower temperature) rather than completely elastic accommodation, then the dislocation structure introduced during deformation will lock the phase boundaries (austenite/martensite), which means that some of the martensite plates will not be able to easily transform back to austenite when the temperature is raised. This means that in the parent, the austenite will have to nucleate inside the martensitic structure during heating. If this is the case we would expect to see an increase in the number of martensite/austenite nucleation sites throughout the material's microstructure. This also explains the reduced volume fraction of martensite in the cycled samples. The increased dislocation density would hinder the temperature-induced twinning to martensite during each cycle of cooling thus giving reduced volume fractions of martensite. As previously discussed in Chapter 2, the twinning process of the microstructure coupled with thermally stress-induced martensite plate growth can be seen as potential contributors to the formation of these nucleation sites, resulting in different mechanical properties. The nucleation growths should be representative in the microstructure possibly as evident nucleation growth sites and grain size difference from one sample to the next, and will be investigated further.

Additionally, it should be noted that literature [49] also indicates that thermally cycling Nitinol does result in an increase in dislocation density which will have an effect on the materials mechanical properties. This will have a similar effect as with cold working

metals; i.e., increasing the materials respective yield and tensile strengths, and reducing the ductility of the material. These have been noted respectively in this study in Table 4.4 listing respective strength properties, and in Figure 4.13 depicting the noted increase in hardness. Referencing the literature [49], it should be noted the thermal cycling profile explored was temperature extremes equivalent to 100°C and -193°C. This study examined a less harsh thermal cycling profile with correlation to medical device applications.

4.4 Microstructural Analysis

4.4.1 Scanning Electron Microscope Micrographs

Figures 4.14 and 4.15 show scanning electron microscope (SEM) images obtained for selected specimens; sample ExovaA being our baseline sample and ExovaB representing the longest cycled cryogenic-temperature treated sample (20 cycles for a total of 160 minutes, as per Table 4.1). SEM images were obtained as well for coupon samples A through D. The samples were polished having been previously etched to reveal the martensitic structure. It can be seen from the two images that there are some distinguishable differences in the grain structure, domain size, and presence of voids in the surface. Using higher magnification, these differences are still apparent, and captured in Figures 4.16 and 4.17.

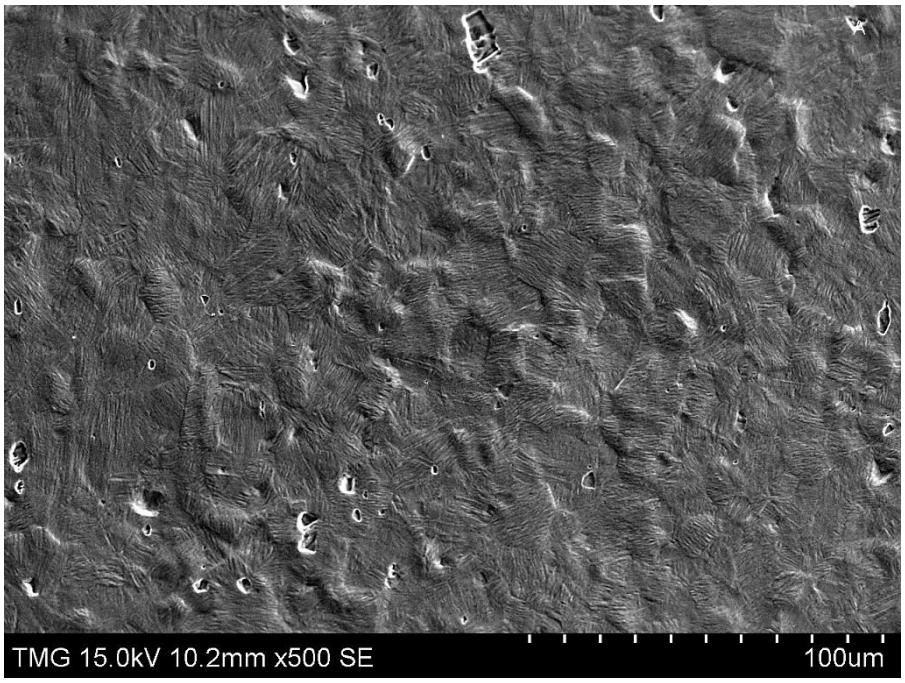

Figure 4.14 SEM micrograph of sample ExovaA (0 cycles), x500 magnification.

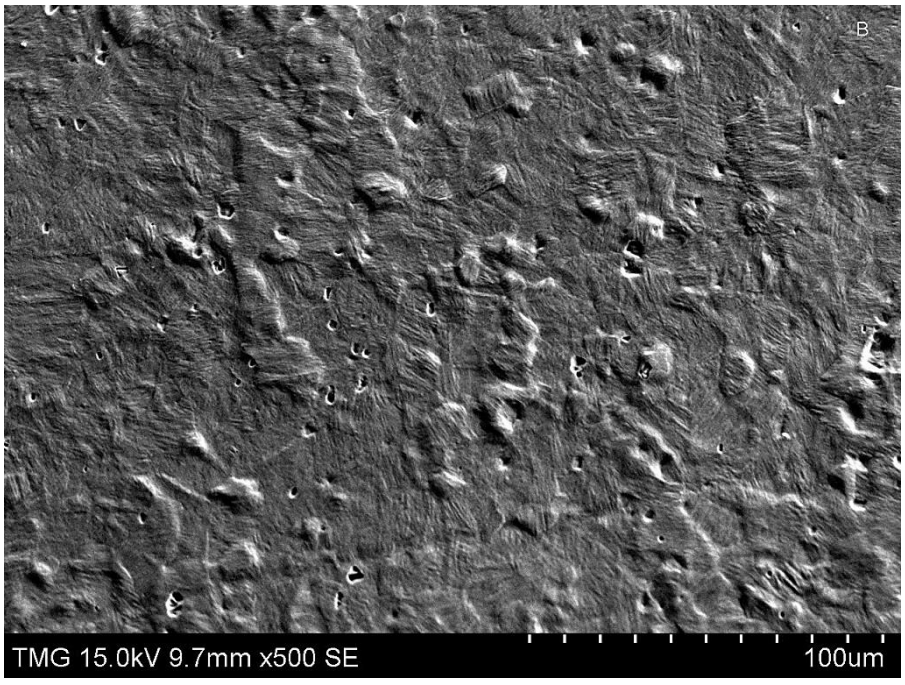

Figure 4.15 SEM micrograph of sample ExovaB (20 cycles), x500 magnification.

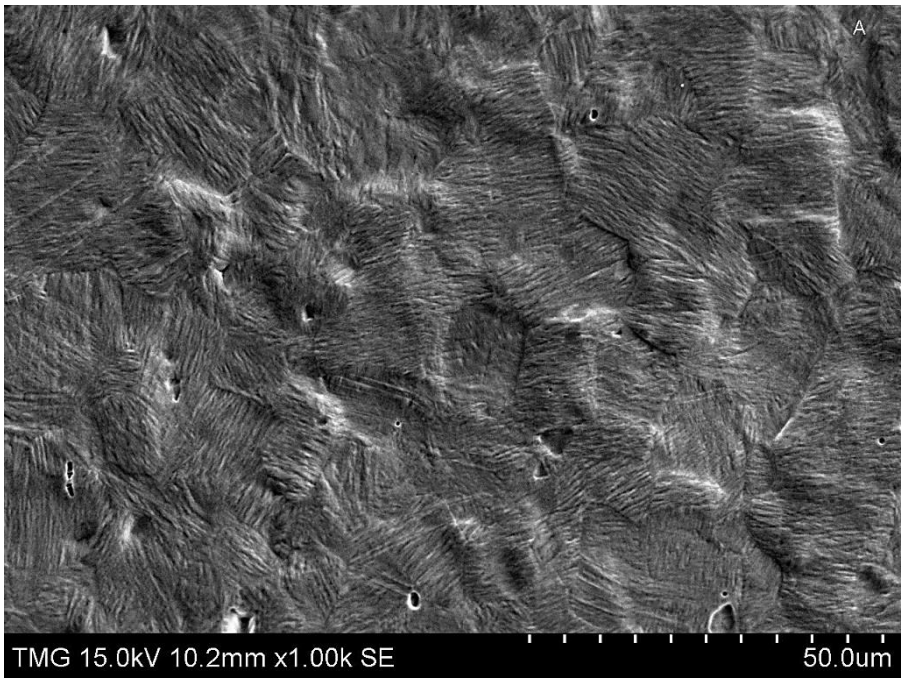

Figure 4.16 SEM micrograph of sample ExovaA (0 cycles), x1.0k magnification.

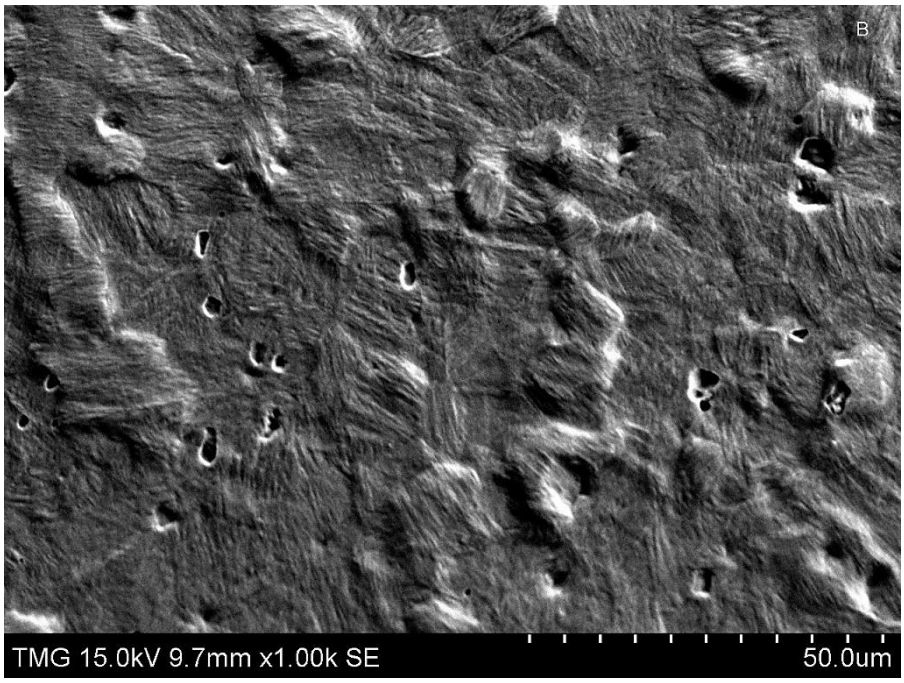

Figure 4.17 SEM micrograph of sample ExovaB (20 cycles), x1.0k magnification.

When comparing both the grain sizes and domains in the cycled sample ExovaB (Figure 4.17) versus the baseline sample ExovaA (Figure 4.16), the respective domains look smaller in size which would correlate to the observed increase in mechanical properties previously discussed in Sections 4.2.2 and 4.2.3.

In order to better enhance the micrograph images for sample ExovaB, the sample was sputter-coated with 70%/30% of Au/Pd. These SEM micrographs are presented in Figures 4.18 through 4.20.

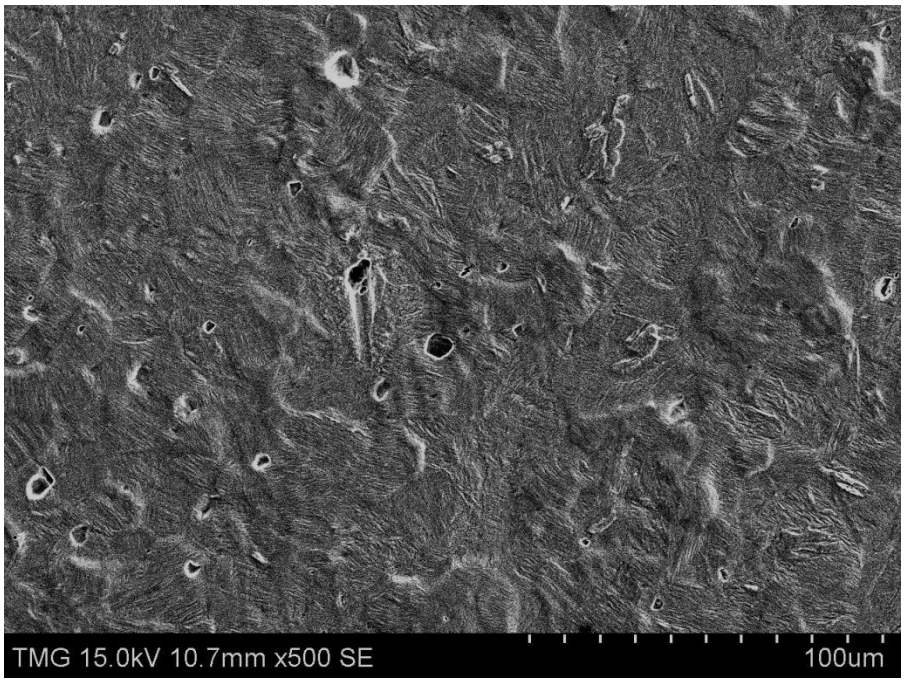

Figure 4.18 SEM micrograph of sample ExovaB (20 cycles), x500 magnification. Nucleation growth site is evident in microstructure at center of image.

As previously thought and can be observed in Figure 4.18, we can see evidence of small microstructural growths throughout the sample, representing nucleation sites. Recall that

sample ExovaB underwent 20 cycles of cryogenic-temperature treatment. As can be seen in Figure 4.20 in more detail, there is evidence of a non-martensitic nucleation site within the structure.

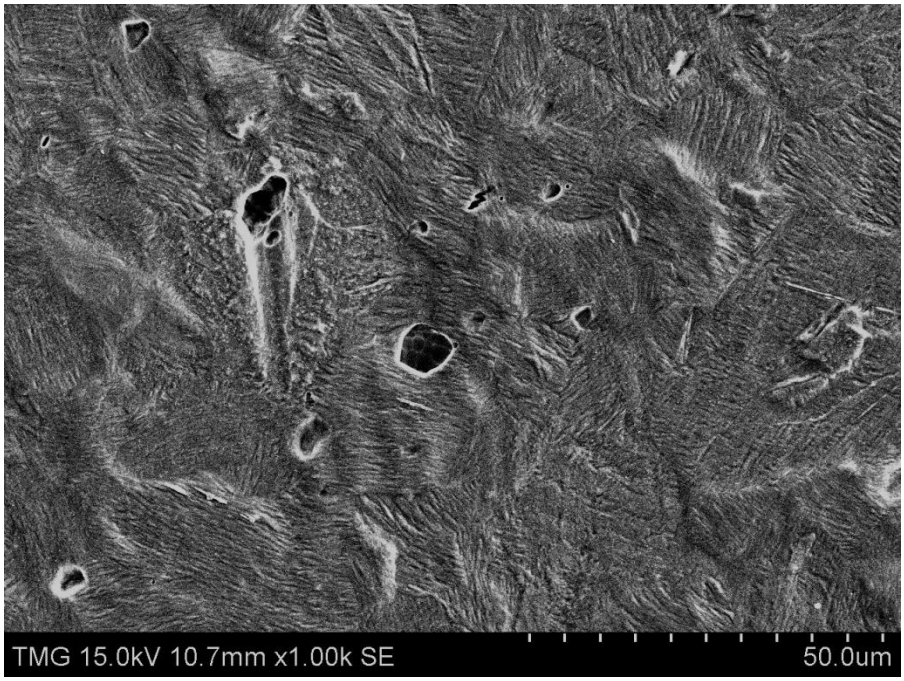

Figure 4.19 SEM micrograph of sample ExovaB (20 cycles), x1.0k magnification. Nucleation growth site is evident in microstructure at center of image.

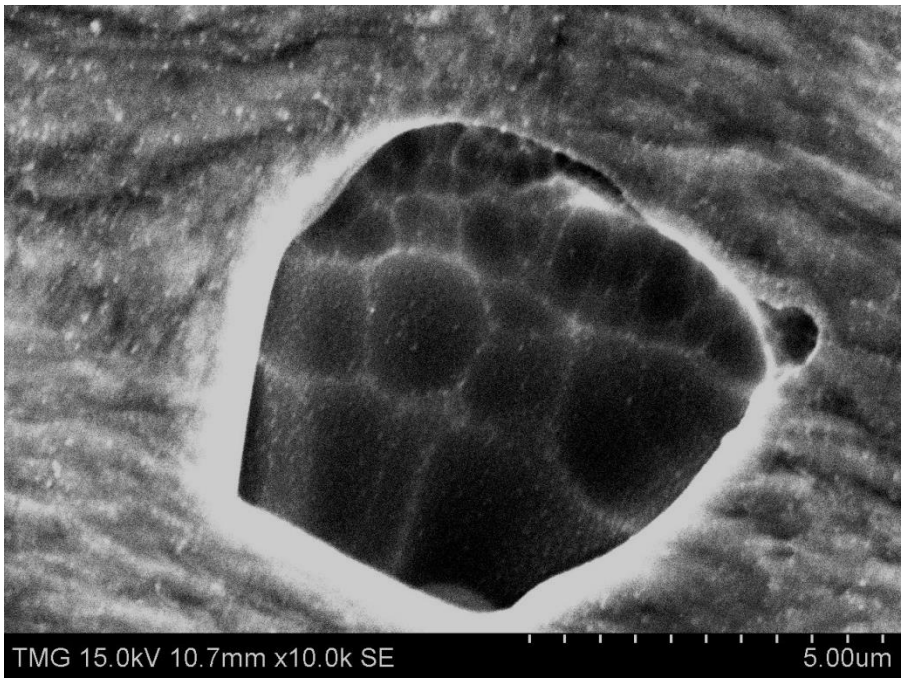

Figure 4.20 SEM micrograph of nucleation growth in sample ExovaB (20 cycles), x10.0k magnification.

Based on the individual grain size and the respective grain distribution, this nucleation would appear to an austenite nucleation zone forming in martensitic structure, as opposed to retained austenite left over from the initial transformation from austenite to martensite during the cooling cycle. Correlating this to steels, as commonly occurs during the quenching of austenitic steel to martensite, a significant proportion of retained austenite is commonly observed. Again, these observed austenitic nucleation growths can be observed throughout the sample ExovaB surface.

4.5 Fractography

4.5.1 Fracture Surface Investigation – Digital Microscope

Fracture surface reconstruction was first carried out in order to better understand the surface fractograph interaction among the samples. Sample images were captured and then digitally stacked and stitched in order to assemble and render composite images of the fracture surfaces. Examples of images captured for sample 9 can be seen in Figures 4.21 and 4.22 below.

As is observed in all the optical fracture surface images reviewed, ductile fracture modes were present in all samples (2-15). No real differences were observed in any of the samples inspected. In order to get a more microscopic view of the fracture surfaces to confirm ductile fracture modes and the presence of respective spherical microvoids, scanning electron microscope fractographs were acquired.

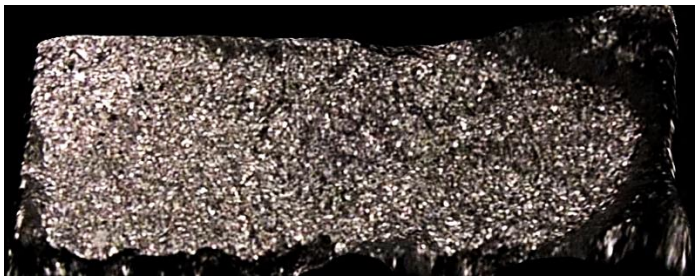

(a)

(b)

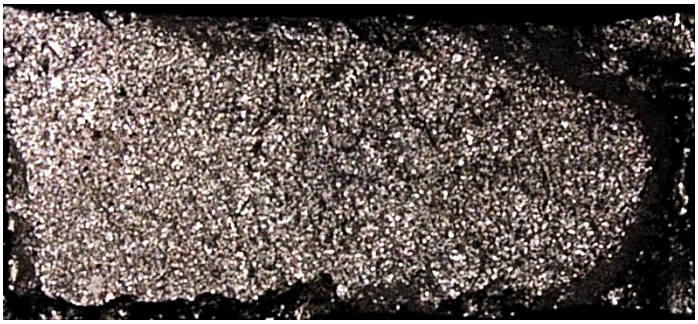

(c)

Figure 4.21 Optical fracture surface side ‘A’ reconstruction for sample 9; images (a) and (b) are isometric perspective views, and (c) is a top view.

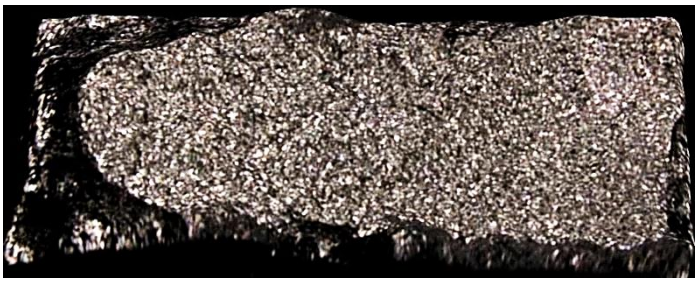

(a)

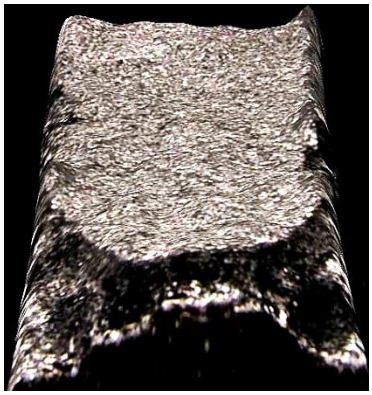

(b)

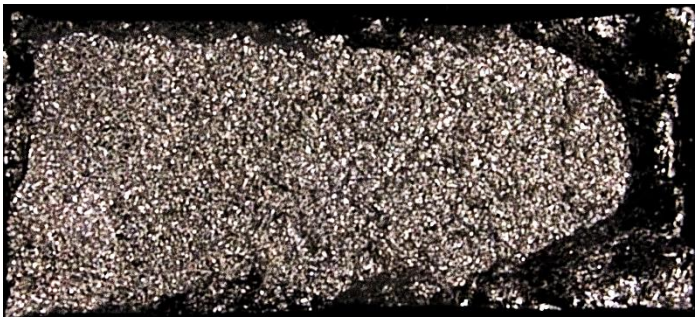

(c)

Figure 4.22 Optical fracture surface side ‘B’ reconstruction for sample 9; images (a) and (b) again are isometric perspective views, and (c) is a top view.

4.5.2 Fracture Surface Investigation – Scanning Electron Microscope

Fractography images were collected for all samples. Examples of images captured for sample 9 can be seen in Figure 4.23 below. Figure 4.24 provides higher magnification SEM fractographs of some specific details of the surfaces, as well as in Figure 4.25 which depicts one of the edges of fracture shown for sample 9. These scanning electron fractographs showed that for all samples, fracture was ductile and confirmed the presence of spherical dimples. This was evident for all samples compared that had steady-state cryo treatments. No real differences were noted.

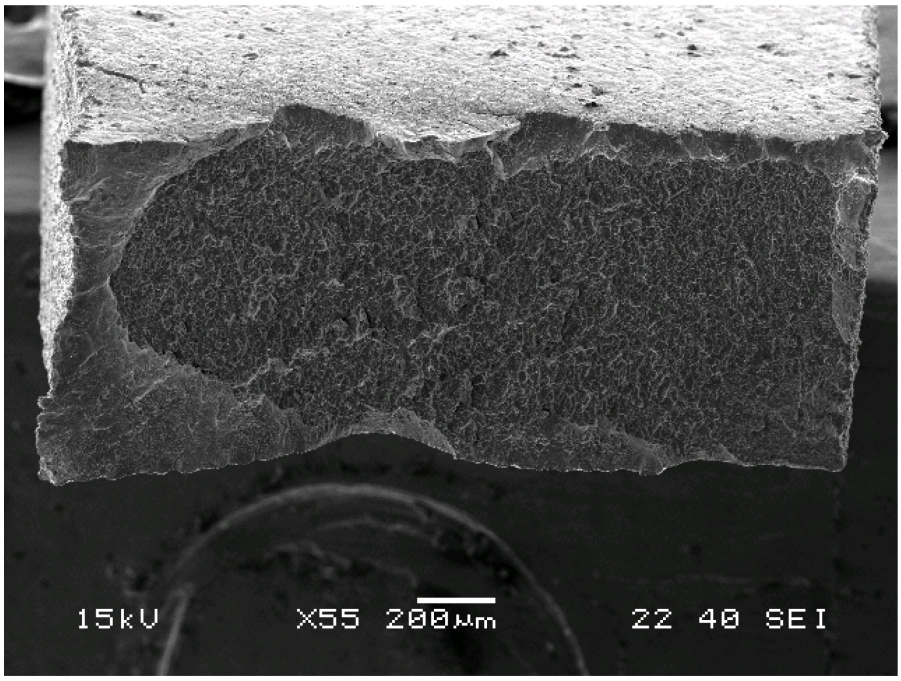

(a)

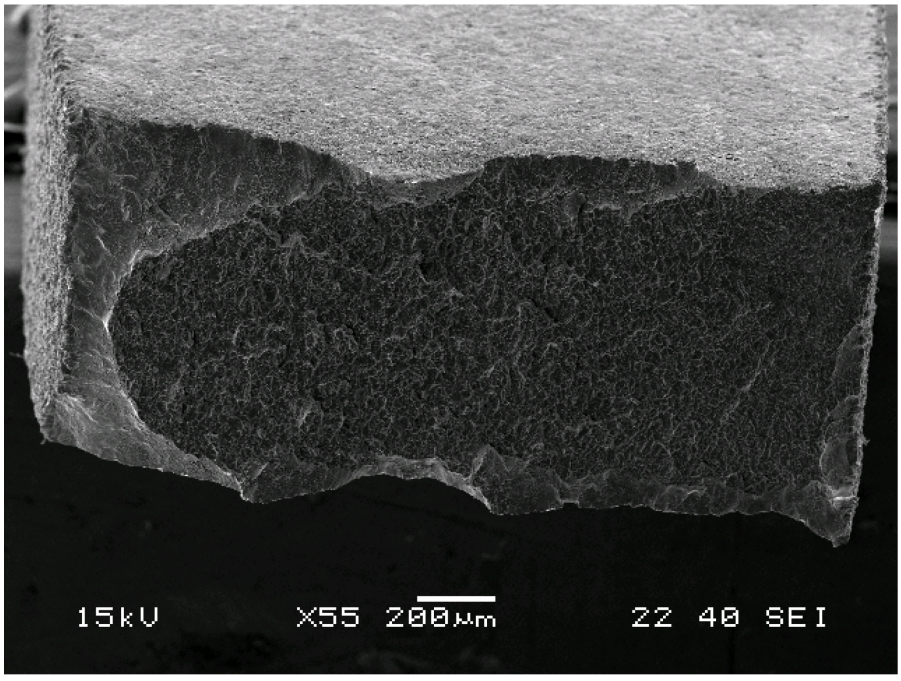

(b)

Figure 4.23 Fracture surface of sample 9; images (a) and (b) represent fracture surfaces 'A' and 'B' respectively of the sample.

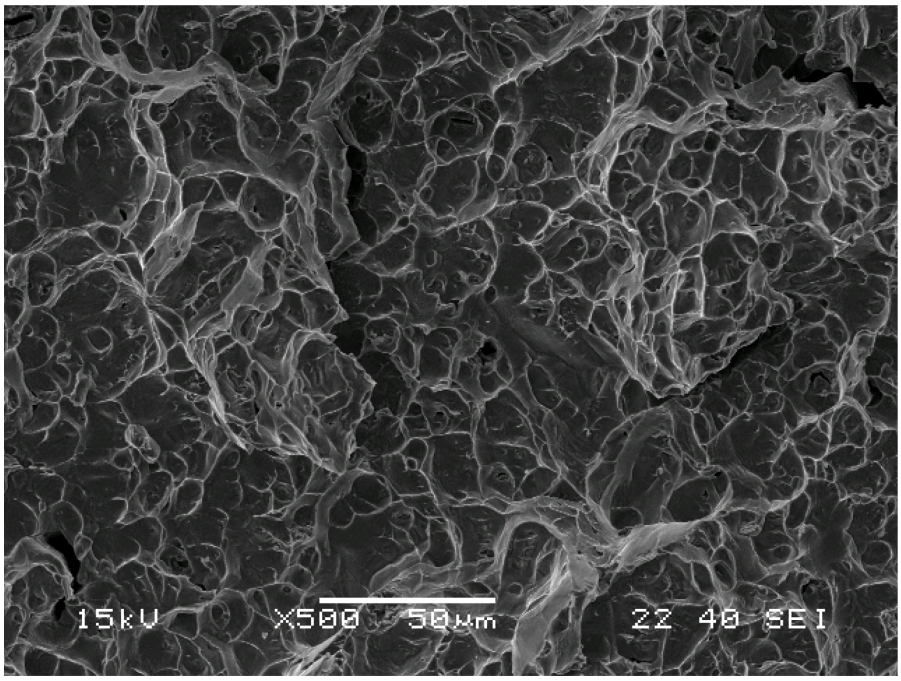

(a)

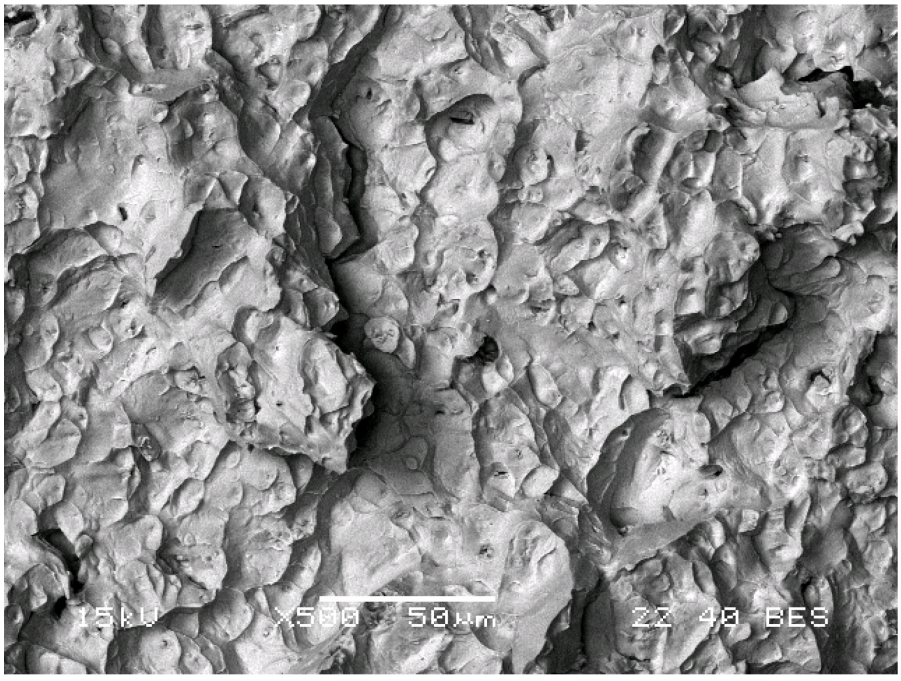

(b)

Figure 4.24 Scanning electron fractographs for sample 9, showing spherical dimple characteristics of ductile fracture; image (a) was produced using secondary electron imaging (SEI) and image (b) was produced using backscatter electron imaging.

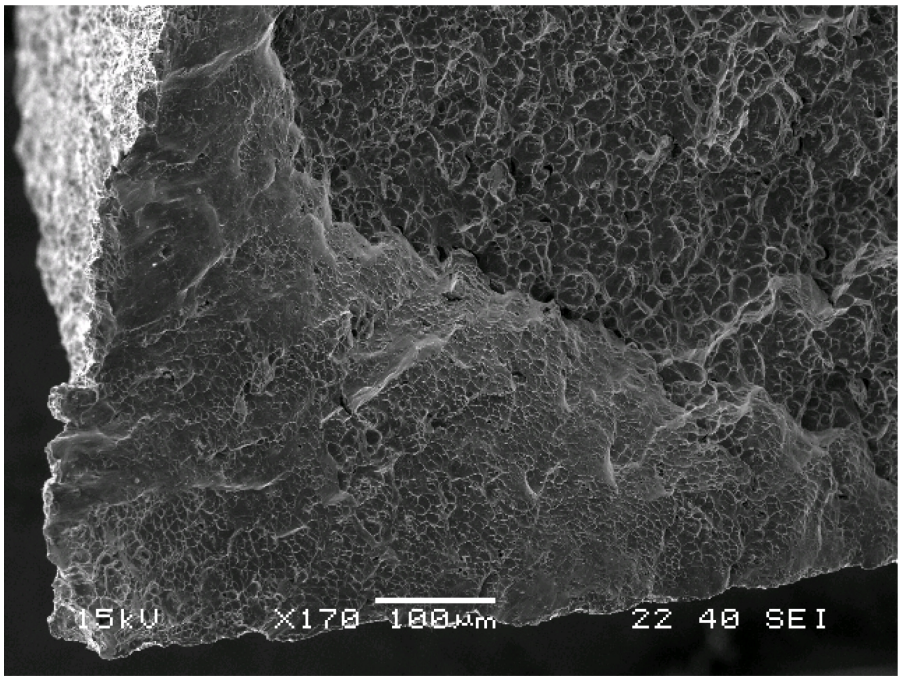

(a)

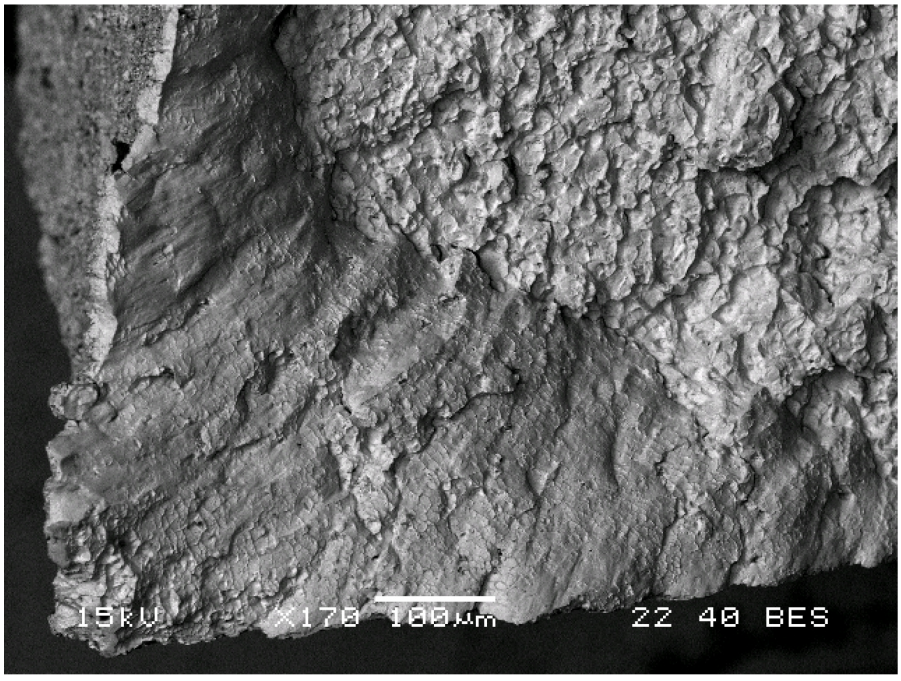

(b)

Figure 4.25 Scanning electron fractographs for a selected edge of fracture for sample 9, again confirming spherical dimples; image (a) was produced using secondary electron imaging, and image (b) was produced using backscatter electron imaging.

Comparing the baseline sample ExovaA (0 cycles) and our high- cycle, cryo-treated sample ExovaB (20 cycles), no observable differences between the two samples were noted. However, this is expected since the observed %elongation difference as seen from Figure 4.9 -- the reduction in elongation for the cycled samples is not very dramatic; approximately 4% elongation is noted and thus it is difficult to observe this from fractographs. This is also apparent when reviewing higher magnification fracture surfaces, which are presented in Figures 4.26 and 4.27 respectively.

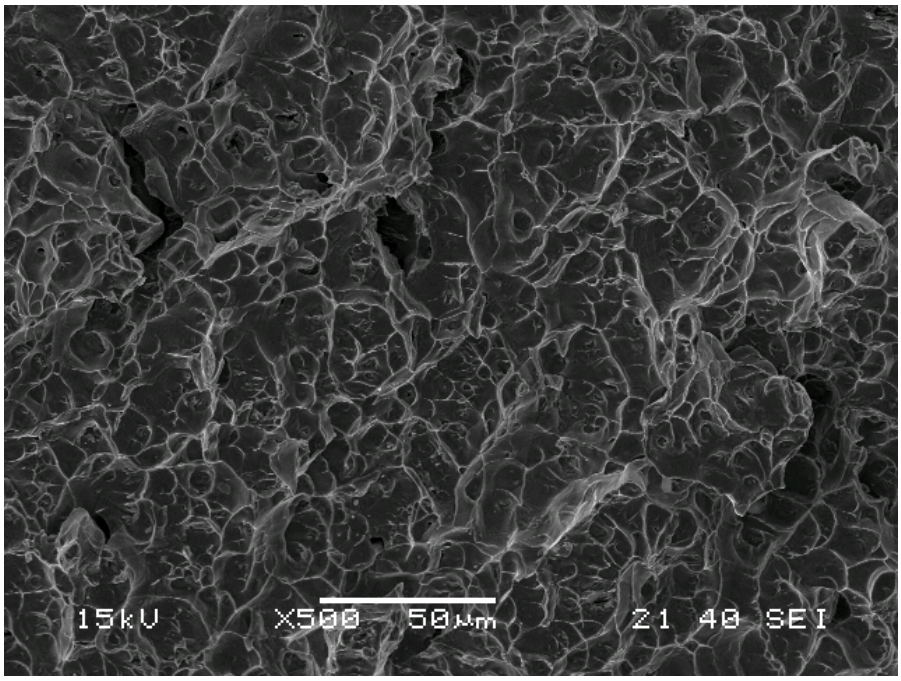

Figure 4.26 Scanning electron fractograph for baseline sample ExovaA (0 cycles).

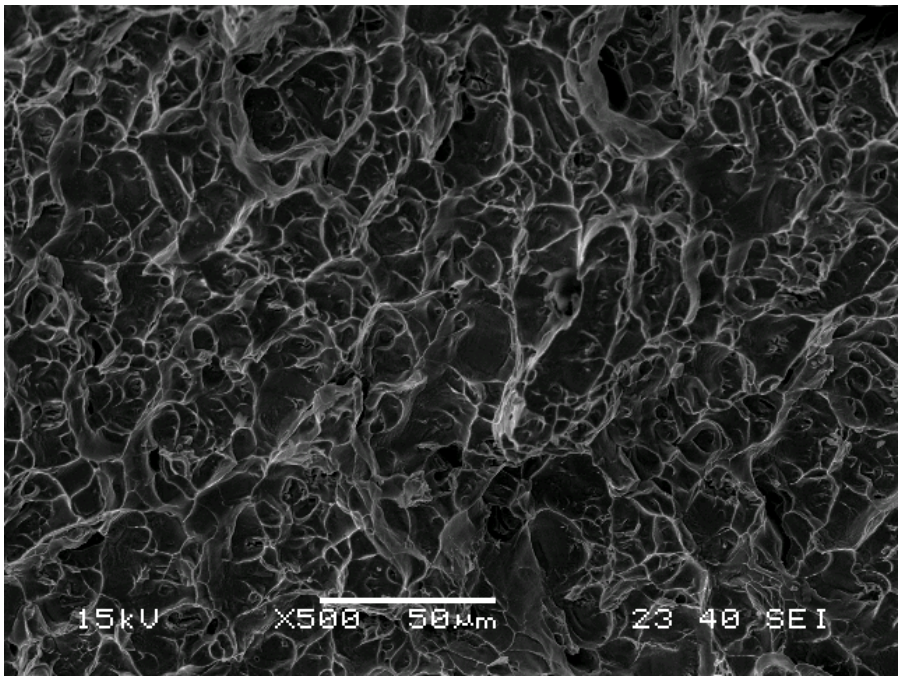

Figure 4.27 Scanning electron fractograph for high-cryo cycled sample ExovaB (20 cycles).

CHAPTER 5

5.1 Conclusions

The purpose and objective of this research was to explore the effects and influence of cryogenic temperatures on the performance and structure of shape memory alloys; specifically, nickel-titanium alloys. This area of interest was primarily analyzed due to the lack of research and experimental data on the subject of shape memory alloy design when exposed to cryogenic environments. Two different modes of cryogenic temperature exposures were examined: steady-state timed cryogenic exposure to -60°C, and cyclically timed cryogenic exposure -60°C and then warmed upwards to +37°C. As a result, the corresponding examined nitinol material responded differently to both treatment types. In summary, this study did confirm that with the application of cryogenic treatments to nitinol shape memory alloys, there was an effect on the material hardness and a slight effect on the materials tensile strength. This was further shown to have a more evident effect when material sample were cryogenically exposed in a cyclical manner versus steady-state.

Findings when exposed to steady-state timed cryogenic exposure will be summarized first, followed by findings when exposed cyclically.

5.1.1 Steady-State Timed Cryogenic Exposure to -60°C

For the superelastic nitinol alloy samples examined, the main mechanical effect of the cryogenic treatment was an evident slight increase in the observed hardness. When comparing steady-state timed exposures to each other, on average, little to no difference was observed. When comparing our control baseline sample and the average hardness values for steady-state timed exposures, the respective sample hardness increased slightly by 2.0%. As for other mechanical properties typical when designing with nitinol shape memory alloys, including thermal hysteresis, they saw no observable differences from sample to sample, and thus can be concluded that the key attributable design properties for nitinol are not affected. This outcome, coupled with the generated and analyzed stress-strain curves having been deemed typical with respect to shape memory alloys, we can conclude that steady-state exposure time duration is not a critical factor.

From a microstructural perspective, when comparing samples exposed to steady-state timed exposures of 32, 64 and 128 minutes, no real noticeable differences were noted. This was also true when comparing each sample to the baseline t=0 sample.

5.1.2 Cyclically Timed Cryogenic Exposure to -60°C and +37°C

For the superelastic nitinol alloy samples examined, again the main mechanical effect of the cryogenic treatment was an evident increase in the observed materials hardness, tensile strength, and estimated final elastic yield strength.

With respect to material hardness, when comparing cyclical exposures of sample set of 32 and 160 minutes, on average, the sample sets resulted in average hardness values of 280.29 kg/mm^2 and 290.40 kg/mm^2, respectively. When comparing our control baseline sample and the average hardness values for the sample cyclically exposed to 160 minutes, the respective hardness increased by 8.7%. With respect to the materials estimated yield strength of martensite, when comparing our control baseline sample to the observed estimated final yield strength for the sample cyclically exposed to 160 minutes, the mechanical property increased by 9.5%. An additional observable difference on mechanical effects was a slight increase in tensile strength. When comparing our control baseline sample to the observed tensile strength for the sample cyclically exposed to 160 minutes, the mechanical property increased by 3.2%. Though not a significant increase, the tendency of the material to display stress-strain curves increasing in tensile strength as cyclically timed exposure durations were also increased is appropriately noted. The increases observed for these described mechanical properties are attributed to both an increase in the formation of austenitic nucleation sites through the materials microstructure, and observed smaller martensitic domains in the grain structure.

From a microstructural perspective, when comparing samples exposed to cyclically timed exposures of 32 and 160 minutes, no real noticeable differences were noted. When comparing micrographs of the baseline t=0 sample to the cryo-cycled sample cycled for 160 minutes, distinguishable differences in both the grain structure and the presence of austenitic nucleation sites were quite evident in the samples microstructure.

5.2 Future Proposed Studies

The effect of cryogenic treatment on nitinol shape memory alloys could be further researched. For example, transmission electron microscopy (TEM) can be utilized to further analyze the possible particles formed due to the sub-zero treatments. Additionally, obtaining further superelastic nitinol alloy samples and exposing to both longer durations of cyclically timed cryogenic exposures and different temperature ranges can further add to the observed behaviors reported here.

REFERENCES

[1] P. Khairy, M. Dubuc, *Cryoablation for Cardiac Arrhythmias*, First edition, Montreal Heart Institute & Medtronic CryoCath LP, Montreal, QC: Vision Communications, 2008. *Please note: all theories and images referenced from this reference are protected by company policies and should be considered proprietary and confidential information.*

[2] P. A. Iaizzo, *Handbook of Cardiac Anatomy, Physiology, and Devices*, Second edition, New York, NY: Springer Science, 2009.

[3] T. W. Duerig, K. N. Melton, D. Stöckel, C. M. Wayman, *Engineering Aspects of Shape Memory Alloys*, First edition, London: Butterworth-Heinemann, 1990.

[4] K. Otsuka, C.M. Wayman, *Shape Memory Materials,* First edition, Cambridge, United Kingdom: Cambridge University Press, 1998.

[5] SAES Memry Inc.; http://www.memry.com/.

[6] W. Callister Jr., *Materials Science and Engineering – An Introduction,* Fifth edition, New York, NY: John Wiley & Sons Inc., 2000.

[7] G. Dieter, *Mechanical Metallurgy,* Third edition, New York, NY: McGraw-Hill, 1986.

[8] J. V. Humbeeck, "Non-medical applications of shape memory alloys", Materials Science & Engineering A, vol. 273-275, pp 134-148, December 1999.

[9] Z.G. Wang, X.T. Zu, Y.Q. Fu, L.M. Wang, "Temperature Memory Effect in TiNi-based Shape Memory Alloys", Thermochimica Acta, pp. 199-205, November 2004.

[10] R. W. Balluffi, S. M. Allen, W. C. Carter, *Kinetic of Materials*, First edition, Hoboken, NJ: John Wiley & Sons Inc., 2005.

[11] P. Marshall, *Austenitic Stainless Steel – Microstructure and Mechanical Properties,* First edition, Essex, United Kingdom: Elsevier Applied Science Publishers, 1984.

[12] A.M. Hall, *Alloys of Iron Research Series: Nickel in Iron and Steel,* First edition, New York, NY: John Wiley & Sons Inc, 1954.

[13] G.F. Comstock, *Alloys of Iron Research Series: Titanium in Iron and Steel,* First edition, New York, NY: John Wiley & Sons Inc, 1955.

[14] K. Bhattacharya, *Microstructure of Martensite: Why it forms and how it gives rise to the shape-memory effect*, First edition, New York, NY: Oxford University Press, 2007.

[15] ASM, Metals Handbook, *Metals Reference Handbook*, Third edition, Metals Park, OH: ASM International, 1993.

[16] ASM, Metals Handbook, Vol. 9, *Metallography and Microstructures*, Metals Park, OH: ASM International, 1990.

[17] K. Otsuka, X. Ren, "Physical Metallurgy of Ti-Ni-based Shape Memory Alloys", Progress in Materials Science, pp. 511-678, 2005.

[18] H.K.D.H. Bhadeshia, R.W.K. Honeycombe, *Steels – Microstructure and Properties,* Third edition, Oxford, United Kingdom: Elsevier Ltd., 2006.

[19] ASM, Metals Handbook, Vol. 1, *Properties and Selection: Nonferrous Alloys and Special-Purpose,* Metals Park, OH: ASM International, 1990.

[20] D. Lagoudas, *Shape Memory Alloys – Modeling and Engineering Applications*, First edition, New York, NY: Springer Science, 2008.

[21] A. Bekker, L. C. Brinson, "Phase Diagram Based Description of the Hysteresis Behavior of Shape Memory Alloys", Acta Materialia, pp. 3649-3665, December 1997.

[22] X. Peng, W. Pi, J. Fan, "A Microstructure-based constitutive Model for the Pseudoelastic Behavior of NiTi Shape Memory Alloys", International Journal of Plasticity, pp. 966-990, July 2007.

[23] F. Auricchio, E. Sacco, "A One-Dimensional Model for Superelastic Shape Memory Alloys with Different Elastic Properties between Austenite and

Martensite", International Journal for Non-Linear Mechanics, pp. 1101-1114, October 1996.

[24] Y. B. Fu, R. W. Ogden, *Nonlinear Elasticity: Theory and Applications*, First edition, Cambridge, United Kingdom: Cambridge University Press, 2001.

[25] C.T. Liu, H. Kunsmann, K. Otsuka, M. Wuttig, *Shape Memory Materials and Phenomena – Fundamental Aspects and Applications,* Pittsburgh, PN: Materials Research Society Symposium Proceedings, Vol. 246, 1991.

[26] D. Helm, P. Haupt, "Shape Memory Behavior: Modelling within continuum Thermomechanics", International Journal of Solids and Structures, pp. 827-849, October 1992.

[27] S. Daly, G. Ravichandran, K. Bhattacharya, "Stress-Induced Martensitic Phase Transformation in Thin Sheet of Nitinol", Acta Materialia, pp. 3593-3600, February 2007.

[28] X.M. He, J.H. Xiang, M.S. Li, S.W. Duo, S.B. Guo, R.F. Zhang, L.J. Rong, "Temperature Memory Effect Induced by Incomplete Transformation in TiNi-based Shape Memory Alloy", Journal of Alloys and Compounds, pp. 338-341, December 2005.

[29] I. Muller, S. Seelecke, "Thermodynamic Aspects of Shape Memory Alloys", Mathematical and Computer Modelling, pp. 1307-1355, 2001.

[30] K. Tanaka, S. Kobayashi, Y. Sato, "Thermomechanics of Transformation Pseudoelasticity and Shape Memory Effect in Alloys", International journal of Plasticity, 59-72, 1986.

[31] V. P. Panoskaltsis, s. Bahuguna, D. Soldatos, "On the thermomechanical Modeling of Shape Memory Alloys", International Journal of Non-Linear Mechanics, pp. 709-722, January 2003.

[32] K. Otsuka, K. Shimizu, "Pseudoelasticity and Shape Memory Effects in Alloys", International Metal Review, pp. 93-114, 1986.

[33] M. Iijima, H. Ohno, I. Kawashima, K. Endo, I. Mizoguchi, "Mechanical Behavior at Different Temperatures and Stresses for Superelastic Nickel-Titanium

Orthodontic Wires having Different Transformation Temperatures", Dental Materials, pp. 88-93, January 2001.

[34] R. Budynas, *Advanced Strength and Applied Elasticity,* Second edition, Boston, MA: McGraw Hill, 1999.

[35] R. Budynas, J.K. Nisbett, *Mechanical Engineering Design*, Eighth edition, New York, NY: McGraw Hill, 2008.

[36] E. Kreyszig, *Advanced Engineering Mathematics,* Eighth edition, New York, NY: John Wiley & Sons Inc., 1999.

[37] J. Perkins, *Shape Memory Effects in Alloys,* Toronto, ON: International Symposium on shape Memory Effects and Applications, Metallurgical Society of AIME, 1975.

[38] K. Wada, Y. Liu, "On the Mechanisms of Two-Way Memory Effect and Stress-Assisted Two-Way Memory Effect in NiTi Shape Memory Alloy", Journal of Alloys and Compounds, pp. 125-128, January 2006.

[39] K. Wada, Y. Liu, "On the Mechanisms of Two-way Memory Effect and Stress-assisted Two-way Memory Effect in NiTi Shape Memory Alloy", journal of Alloys and Compounds, pp. 125-128, January 2006.

[40] F. Auricchio, S. Marfia, E. Sacco, "Modelling of Shape Memory Alloy Materials: Training and Two-way Memory Effects", Computers and Structures, pp. 2301-2317, July 2003.

[41] ASM, Metals Handbook, Vol. 3, *Alloy Phase Diagrams*, Metals Park, OH: ASM International, 1990.

[42] D.S. Ford, S. R. White, "Thermomechanical Behavior of 55Ni45Ti Nitinol", Acta Metallugica, vol. 44, No. 6, pp 2295-2307, 1996.

[43] H.R. Chen, *Shape Memory Alloys: Manufacture, Properties and Applications*, First edition, New York, NY: Nova Science Publishers, Inc., 2010.

[44] ASTM F2005 - 05 Standard Terminology for Nickel-Titanium Shape Memory Alloys.

[45] ASTM F2063 - 05 Standard Specification for Wrought Nickel-Titanium Shape Memory Alloys for Medical Devices and Surgical Implants.

[46] ASTM E8 / E8M - 08 Standard Test Methods for Tension Testing of Metallic Materials.

[47] K. Gall, J. Tyber, G. Wilkesanders, S. W. Robertson, R. O. Ritchie, H. J. Maier, "Effect of microstructure on the fatigue of hot-rolled and cold-drawn NiTi shape memory alloys", Materials Science and Engineering A, pp. 389–403, 2008.

[48] ASTM F2004 - 05 Standard Test Method for Transformation Temperature of Nickel-Titanium Alloys by Thermal Analysis.

[49] A.R. Pelton, G.H. Huang, P. Moine, R. Sinclair, "Effects of thermal cycling on microstructure and properties in Nitinol", Materials Science and Engineering A 532 pp. 130– 138, 2012.